Journal of Structural Geology 187 (2024) 105231

Contents lists available at ScienceDirect

Journal of Structural Geology

journal homepage: www.elsevier.com/locate/jsg

3D study of dyke-induced asymmetric graben: The 1971 Mt. Etna (Italy) case by structural data and numerical modelling

Fabio L. Bonali [a,b,*], Noemi Corti [a], Federico Pasquaré Mariotto [c], Emanuela De Beni [d], Sofia Bressan [a,1], Massimo Cantarero [d], Elena Russo [a], Marco Neri [d], Alessandro Tibaldi [a,b]

[a] Department of Earth and Environmental Sciences, University of Milan-Bicocca, Milan, Italy
[b] CRUST – Interuniversity Centre for 3D Seismotectonics with Territorial Applications, Chieti, Italy
[c] Department of Human and Innovation Sciences, Insubria University, Como, Italy
[d] Istituto Nazionale di Geofisica e Vulcanologia, Osservatorio Etneo, Sezione di Catania, Catania, Italy

ARTICLE INFO

Keywords:
Dyke-induced graben
Faults
Photogrammetry
Etna
Modelling

ABSTRACT

In this work, we have integrated field data and numerical models to characterise a unique dyke-induced graben system, exposed both in section and plan view, with an unexpected asymmetric fault geometry. This volcano-tectonic feature is related to the 1971 eruption of Mt. Etna (southern Italy) and is located near the northern wall of the Valle del Bove, a huge depression carved into the eastern flank of the edifice. A new structural map and quantitative data were obtained from the analysis of aerial stereophotos collected before the onset of the 1971 eruption and after, high-resolution drone-derived models and field surveys carried out in the summer of 2022. In plan view, the graben is 2-km-long and its width ranges 27–143 m from the bottom to the upper part of the section view, with about 82 m of difference in elevation from top to bottom. Graben faults clearly show an asymmetric setting in terms of attitude, with one fault that dips 70° to the south, and the other one that dips 50° to the north. Vertical offset values are greater at higher elevations. We also ran a set of numerical models, aimed at investigating the distribution and orientation of stresses around the inferred dyke tip and in the host rock. The comparison between field data and numerical models suggests a key role of the inclined topography, as shown in section view, in determining the orientation of dyke-induced σ_1 and σ_3 in the host rock. This, in turn, controls the geometry of the graben faults, resulting in the observed asymmetric setting. Additionally, dyke-induced stress concentrations and vertical offset values support the hypothesis of a downward propagation of the graben faults, from the surface down to the dyke tip.

1. Introduction

Extensional structures such as fissures, normal faults and grabens, can be produced by regional tectonic processes (Thatcher and Hill, 1995; Rowland et al., 2007), as well as by dyke injection in volcano-tectonic regimes (e.g. Wright et al., 2006; Sigmundsson et al., 2015). During dyke propagation, tensile stress concentrates above the dyke tip due mainly to magma overpressure (P_o) (Gudmundsson, 2011a; Drymoni et al., 2021), favouring Mode I fracturing in the host rock (Griffith, 1924; Anderson, 1951; Broek, 1982; Rubin and Pollard, 1987; Rubin, 1995). According to Griffith's theory (Griffith, 1924), previous research suggests that a dry fracture segment may form at the surface (Broek, 1982; Warpinski, 1985; Bonafede and Olivieri, 1995; Garagash and Detournay, 2000; Billi et al., 2003; Tibaldi, 2015; Drymoni et al., 2021; Tibaldi et al., 2022), or magma can propagate into the newly-formed fracture (Anderson, 1951; Rubin, 1995).

P_o also generates shear stress that affects the host rock along the upper sides of the propagating dyke (Gudmundsson, 2011a). This produces deformation that can reach up to the topographic surface, resulting in the formation of faults and grabens (e.g. Warpinski, 1985; Rubin and Pollard, 1988; Bonafede and Olivieri, 1995; Garagash and Detournay, 2000; Billi et al., 2003; Tibaldi, 2015; Tibaldi et al., 2022). A symmetric graben can form in the case of a vertical dyke, with two maxima of surface ground breaking, one on each side of the dyke plane. Pollard et al. (1983) and Mastin and Pollard (1988) suggested that the two maxima are separated by a distance roughly equal to twice the

* Corresponding author. Department of Earth and Environmental Sciences, University of Milan-Bicocca, Milan, Italy.
E-mail address: fabio.bonali@unimib.it (F.L. Bonali).
[1] Now at Department of Geosciences, University of Padova, Padova, Italy.

https://doi.org/10.1016/j.jsg.2024.105231
Received 16 November 2023; Received in revised form 1 August 2024; Accepted 7 August 2024
Available online 15 August 2024

depth of the dyke top - the so-called "dyke rule". An inclined sheet would instead produce the development of a half-graben structure (Pollard et al., 1983; Mastin and Pollard, 1988; Bazargan and Gudmundsson, 2020; Tibaldi et al., 2022; Drymoni et al., 2023).

In recent years, several studies have been carried out to shed light on the relationship between dykes and the related surface deformation. One approach includes field observations integrated by aerophotogrammetric analyses (e.g. Rubin and Pollard, 1988; Billi et al., 2003; Neri et al., 2011; Tibaldi et al., 2020a, 2022), which guarantee high precision at the scale of the outcrop. In the last decades of the 1900s, the advent of geodetic analysis provided the picture of the deformation field in very large areal settings (e.g. Casu et al., 2006; Neri et al., 2007; Bonforte et al., 2009, 2011; Grandin et al., 2010; Ruch et al., 2016) even if measurement of the deformation near the sources is difficult due to the high magnitude of the deformation itself, generating decorrelated interferograms (De Novellis et al., 2019, and refs therein). Field mapping and geodetic analyses are, therefore, intrinsically complementary and both are necessary to study such a phenomenon. Surface dyke-induced deformation is also commonly studied by numerical (e.g. Gudmundsson, 2020; Drymoni et al., 2021) and analogue modelling (e.g. Trippanera et al., 2014, 2015a; Galland et al., 2015; Guldstrand et al., 2017). Field data and geodetic analyses usually provide a good picture of the surface deformation in plan view (e.g. Nobile et al., 2012; Xu et al., 2016; Tibaldi et al., 2020a, 2022), whereas numerical and analogue modelling usually explore a number of scenarios for a better understanding of the relationship between dyke geometry and depth, layering, fault growth and surface graben formation also in section view (e.g. Rubin and Pollard, 1988; Gudmundsson, 2003; Al Shehri and Gudmundsson, 2018; Drymoni et al., 2022; Clunes et al., 2023).

In the present work, we highlight a unique case of a dyke-induced graben fully exposed in both plan and section view, contributing to unravelling the complex relationship between the various intervening parameters. This graben formed during the eruptive event of 1971 A.D., as a result of a lateral dyke propagation, and is located along the northern wall of the Valle del Bove (VdB), a huge depression cut into the eastern flank of Mt. Etna, southern Italy (Calvari et al., 2004, Fig. 1). This area is located within a block that moves homogeneously towards the ESE, based on the data from Bonforte et al. (2011). We wish to point out that, in our case study, we have a complete view of the lithostratigraphy of the studied rock volume, as well as of the fault geometry and offset, including its variation with depth, as observed in the field in section view (Ferrari et al., 1991; Neri et al., 1991, 2011; Coltelli et al., 1994; Branca et al., 2011a, and refs therein). We used these ground truth data as inputs for Finite Element Method (FEM) numerical modelling. This is different from previous works, where subsurface fault geometry was inferred by the inversion of geodetic data (e.g. Wright et al., 2006; Grandin et al., 2009; Pallister et al., 2010; Nobile et al., 2012) together with earthquakes hypocentres (Calais et al., 2008), or by seismic reflection data for deeper dykes (Magee and Jackson, 2021).

We have fully characterised our case study with the aid of

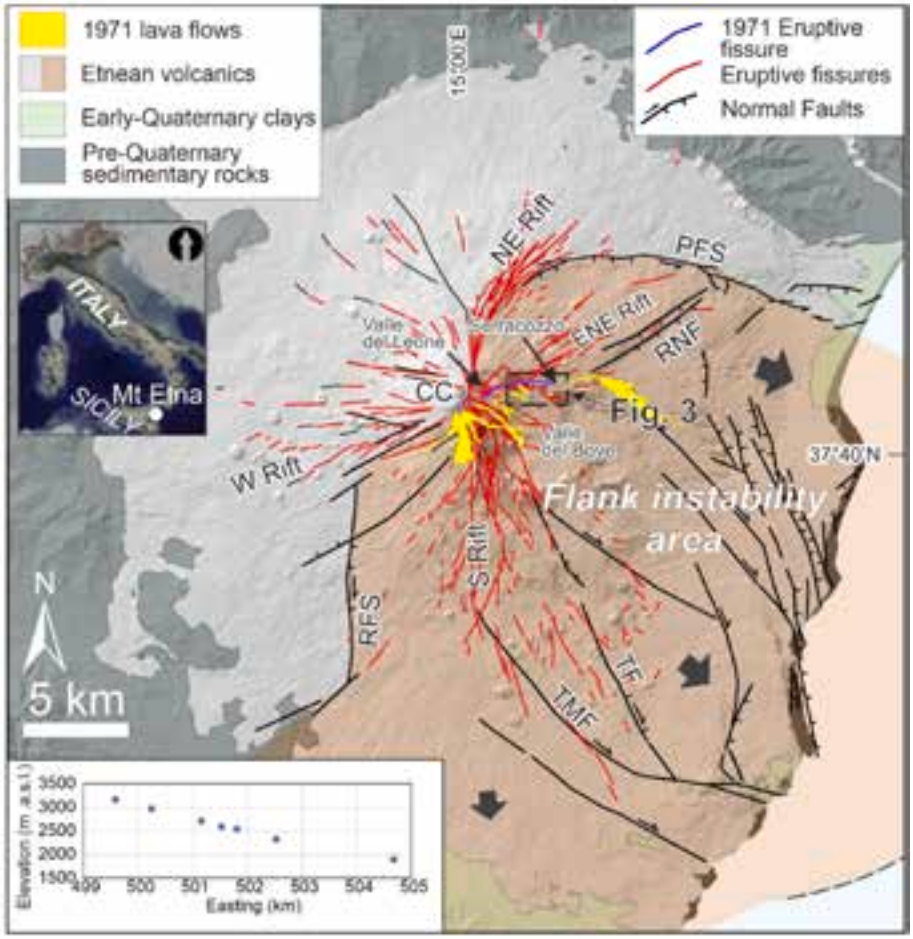

Fig. 1. Map showing the main volcanotectonic features of Mt. Etna: the 1971 lava flows are represented by yellow polygons, whereas the eruptive fissure system is shown by blue lines. Arrows indicate directions of movement of different portions of the zone affected by flank instability-induced displacement. The dotted rectangle highlights the study area. CC: central craters; RNF: Ripe della Naca normal faults; PFS: Pernicana fault system; RFS: Ragalna fault system; TF: Trecastagni fault; TMF: Tremestieri fault (modified after Neri et al., 2011; Branca et al., 2011a, 2021). The inset shows the elevation of the 1971 vents with respect to the easting. (For interpretation of the references to colour in this figure legend, the reader is referred to the Web version of this article.)

geomorphological and structural field observations, data from historical aerial stereophotos collected before the onset of the 1971 eruption and after, as well as from drone surveys, carried out in the summer of 2022. In detail, we have placed special emphasis on the development of an asymmetric graben cropping out in section view, a poorly studied topic. Afterwards, we performed a series of numerical models to investigate the distribution and orientation of stress ahead of the dyke tip, when the latter interacts with the local morphotectonic setting. We evaluated the effects of dyke-induced stresses in the host rock with respect to graben fault geometry, considering: *i)* different dyke dip values (75° and 90°); *ii)* horizontal and inclined (25°) topography; *iii)* homogeneous and heterogeneous host rock, assigning different mechanical properties to the volcanic layers, according to the lithostratigraphic succession observed in the field between the dyke and the surface.

2. Geological background

Mt. Etna is a huge basaltic composite stratovolcano formed during the last 500 ka in eastern Sicily (Italy). Its geological evolution is divided in four main evolutionary phases of eruptive activity, of which the Stratovolcano phase (60 ka-Present) is the most recent (details in Branca et al., 2011a; Barreca et al., 2018). Our study area is located immediately NE of the northern escarpment of the VdB (Fig. 1), and comprises part of the VdB floor and the escarpment, as well as part of the E flank (Figs. 1, 2A and 3). The outcrop along the VdB escarpment clearly exposes volcanic products related to the Ellittico volcano (60-15 ka ago) and units related to the activity of the last 15 ka, belonging to Mongibello volcano (details on the stratigraphic succession are shown in Fig. 2B). Such succession is nowadays mainly covered by metres of historical and recent pyroclastic fall deposits, still belonging to the Mongibello volcano (Branca et al., 2011a, b), in areas with shallow-dipping slopes.

The 1971 dyke propagated within the eastern flank of the volcano (Fig. 1), specifically along the so-called ENE Rift zone, which is characterised by a swarm of dry fractures and eruptive fissures (or monogenetic cones), mostly striking in the N70-90°E range (Azzaro et al., 2012) at about 2300-1600 m a.s.l. Another important rift zone where the eruptive fissures of Mongibello volcano are spatially clustered is the NE Rift (Fig. 1) (Kieffer, 1975, 1985; Lo Giudice et al., 1982; McGuire and Pullen, 1989; Garduño et al., 1997; Monaco et al., 2010; Patanè et al., 2011; Azzaro et al., 2012; Cappello et al., 2012; Ruch et al., 2012). Rift zones of Mt. Etna represent ideal locations for magma rising and lateral propagation, leading to flank (or lateral) eruptions, which are usually fed by shallow (1–3 km) dykes propagating from the central conduit (Acocella and Neri, 2009). During historical times, several fissure eruptions affected the ENE Rift (1865, 1928, 1971), the most recent of which occurred in 1979 (Branca et al., 2011a). Here, we focus on the easternmost part of the eruptive fissure system associated with the 1971 eruption (Fig. 1), an area where the formation of a series of eruptive fissures and dry fractures was reported by Le Guern (1972) in a 1:10,000 map. Dry fractures were successively classified into a series of normal faults, delineating a graben that also affects the VdB rim, as reported in the literature at a scale of 1:5000 (Coltelli et al., 1994).

Temporally, the 1971 eruption was articulated in two main time

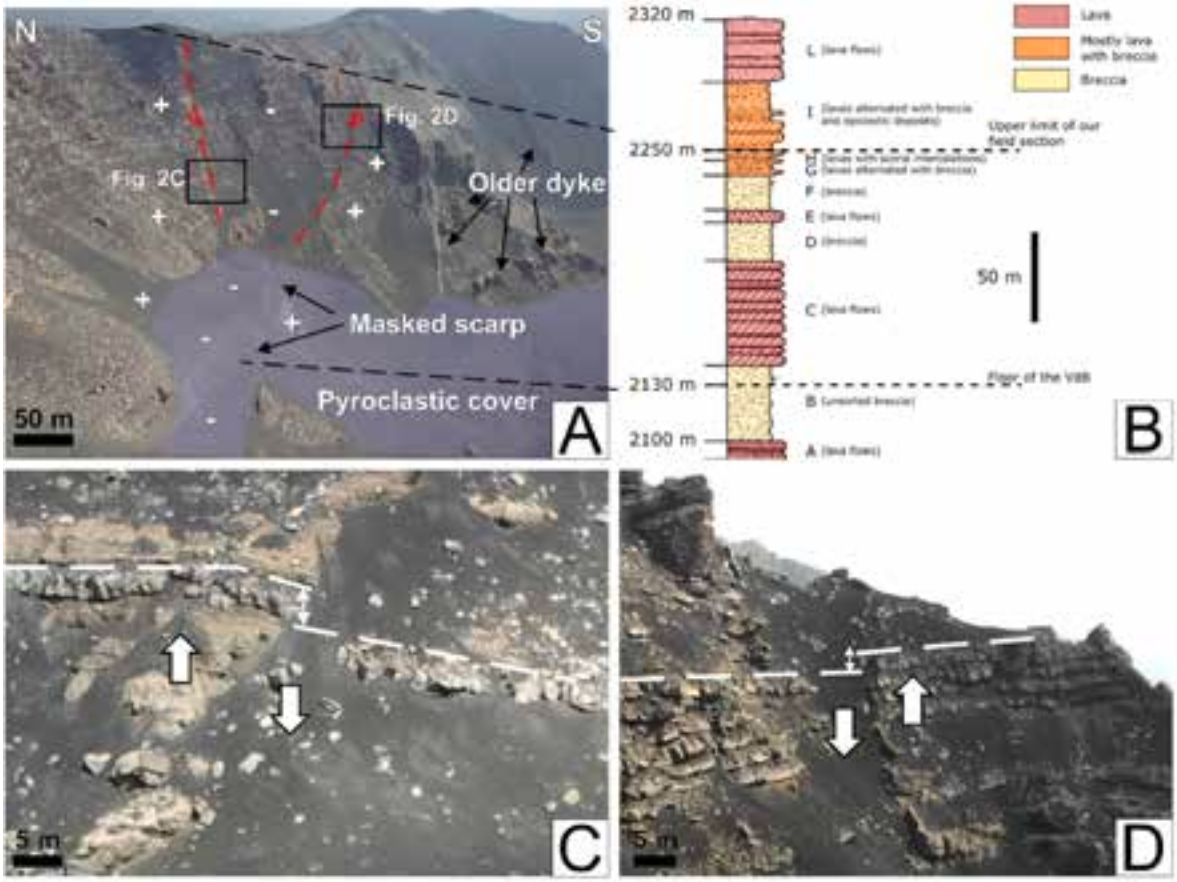

Fig. 2. (A) Drone-captured picture showing the dyke-induced graben in section view. The downthrown block is highlighted with the negative symbol; normal faults are also shown. The fault scarps affecting the VdB floor are presently covered by recent pyroclastic deposits. (B) Detailed stratigraphic column of the area of the VdB affected by the graben, modified after Branca et al. (2011a). Units are summarised from a mechanical point of view, following the approach of Drymoni et al. (2023). Units A-I represent subunits of the Serra delle Concazze Formation of the Ellittico Volcano (60–15 ka). Unit L belongs to the Pietracannone formation of the Mongibello Volcano (last 15 ka). (C–D) Closer drone-captured pictures showing offset markers, represented by contacts between lava and pyroclastic deposits.

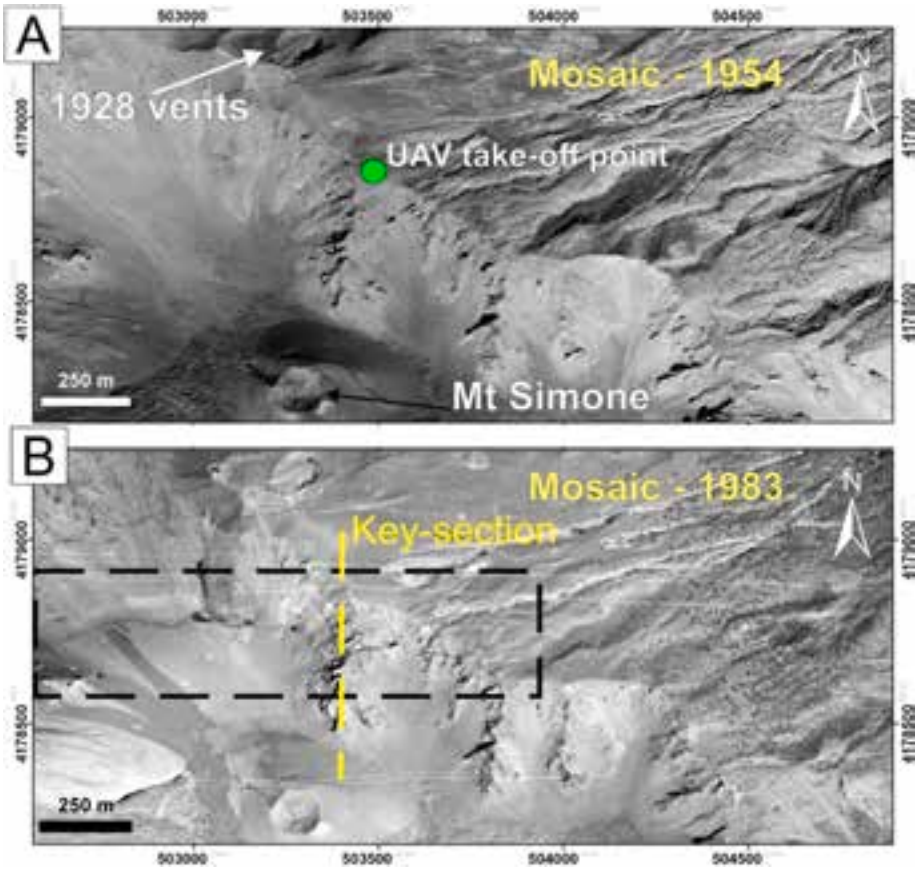

Fig. 3. OMs based on historical aerial photographs from 1954 (A) and 1983 (B), respectively. The black rectangle shows the study area of the present research where the graben faults developed due to dyke intrusion. The green circle in Fig. 3A represents the take-off location for UAS/UAV missions. Ref. system: UTM33/WGS84. (For interpretation of the references to colour in this figure legend, the reader is referred to the Web version of this article.)

intervals: 5 April-6 May and 7 May-12 June (all details on the eruption are summarised in Branca et al., 2021). During the first stage, volcanic activity affected the southern and eastern part of the summit crater, at an elevation of about 3000 m a.s.l. (Fig. 1). During the second stage, a WSW-ENE-trending fracture system developed from about 2900 m a.s.l. towards the Valle del Leone, associated with the opening of five eruptive vents, located between 2680 and 2300 m a.s.l., with lava flows emplaced in the VdB (Fig. 1). The ENE migration of the feeder dyke, as long as 4.5 km in total, reached as far as the northern wall of the VdB at Serra delle Concazze, resulting in the opening of two short eruptive fissures on the E flank at a lower elevation (1840 and 1800 m a.s.l., at Serracozzo) during the night of 11–12 May; the fissures were characterised only by effusive activity, with lava flows that expanded on the eastern flank for 7 km, stopping at about 600 m a.s.l. (Fig. 1) (Branca et al., 2021). As reported in the geological map (Branca et al., 2011a), and as highlighted with a greater detail on the orthomosaic derived from historical photos from 1983 (Fig. 3), this dyke propagation resulted in the formation of a graben that is still well preserved and can be clearly observed in section view on the northern wall of the VdB (Fig. 2). Differently, in plan view, the graben is nowadays totally covered by recent pyroclastic deposits on the E flank, and partially covered on the VdB floor (Fig. 2A).

3. Methodology

Being located half along the E-flank of Mt. Etna and half on the VdB floor and rim (Figs. 1 and 2A), the study area is a rough and dangerous terrain. In addition, it is presently covered by metres of recent pyroclastic deposits emitted over the last 50 years by eruptions from the summit vents of Mt. Etna. To cope with the above limitations, we came up with the following: *i)* as a first step, we analysed two sets of historical aerial photos, prior and after the event, to better locate and characterise the dyke-induced faults (Fig. 3A–B); *ii)* we performed an Unmanned Aerial Vehicle (UAV)/Unmanned Aircraft System (UAS) survey to create a high-resolution 3D dataset (orthomosaic, Digital Surface Model and 3D Tiled Model) for quantitative data collection along the VdB wall; *iii)* we conducted classical field investigations, wherever possible, to locate the graben faults; *iv)* lastly, we ran numerical models to gain insight into dyke-induced stresses, considering different geometrical and mechanical conditions.

3.1. Mapping of graben faults from historical aerial photos

First, we precisely identified the area subject to the formation of a graben structure related to the 1971 dyke propagation. To achieve this goal, we applied a *'time machine approach'* by studying sets of historical photos taken closely to the event. We selected a total of 20 historical aerial photos from 1954 to 1983, ten per each year, which were studied in stereoscopic view. Through Structure-from-Motion (SfM) photogrammetry processing (e.g. Schiefer and Gilbert, 2007; Gomez et al., 2015), the photos were used to produce two high-resolution orthomosaics (OMs) for the area with a resolution of 29.0 and 19.5 cm/pixel, respectively (Fig. 3A–B). The original historical photos were bought from the Istituto Geografico Militare (IGM) (https://www.igmi.org/) at a resolution of 2400 DPI, in a TIFF image format. Photogrammetry processing was performed through a commercial SfM software, Agisoft Metashape (http://www.agisoft.com/), with medium quality settings for the alignment and for the dense cloud building process. 15 Ground Control Points (GCPs) were collected from the topographic map of 1955, over an area of 9 × 5 km, and used to reference both OMs. The overall quality of the historical photos allowed us to produce reliable OMs,

differently from Digital Surface Models (DSMs) that are not reliable enough in terms of accuracy to collect quantitative data on the vertical offset of the fault scarps. The comparison of the two OMs enabled us to produce a structural map for the 1971 dyke-induced fracture field with the highest detail possible, useful to plan both the drone survey and field checks, as well as collect quantitative measurements, such as the width of the graben along its entire length.

3.2. Quantitative data collection from 3D models and field surveys

Quantitative data regarding faults attitude and vertical offset were mainly collected from high-resolution models derived through photogrammetry processing. To obtain a high-resolution DSM and OM of the VdB wall, we firstly applied the SfM photogrammetry technique through UAS surveys. Regarding pictures collection, we followed an overall workflow that had already been applied in volcanic terrains and in challenging logistic conditions (all details in Bonali et al., 2019, 2021). Additionally, due to the harsh logistic conditions, we used the DJI Phantom 4 PRO – camera sensor of 20 MP -, equipped with Real Time Kinematic (RTK) to obtain precisely referenced models without adding GCPs across the area (e.g. De Beni et al., 2024), even if those are recommended for a better scaling and referencing of the SfM-derived models as well as to avoid any bulging effect (James and Robson, 2012; Turner et al., 2012; Westoby et al., 2012; Smith et al., 2016; Vollgger and Cruden, 2016; Esposito et al., 2017; James et al., 2017). Flight height was set to 80–95 m above the starting point, located along the VdB rim (Fig. 3A), reaching the pixel size of about 5.5 cm/pixel for the resulting 3D Tiled Model (Fig. 4B) and OM (Fig. 5B), and of 11 cm/pixel for the DSM (Fig. 5A). In greater detail, the flights were conducted at 95 m outside the VdB area and at 80 m above the take-off point within the VdB area, to minimize the difference in ground sample distance (GSD); the overlap ratio was set up to 85% and 80% along the flight path and in a lateral direction, respectively (Gerloni et al., 2018; Antoniou et al., 2019; Bonali et al., 2019, 2021; Fallati et al., 2020). For the photogrammetry processing of the 656 captured pictures, we used Agisoft Metashape, commonly used thanks to the high quality of the resulting output models (Benassi et al., 2017; Burns and Delparte, 2017; Cook, 2017). The processing was articulated in a few key steps (workflow), described in detail by Verhoeven (2011), Brunier et al. (2016) and Tibaldi et al. (2020b), which led to the creation of the DSM, the orthomosaic and the 3D Tiled model as final products (Fig. 5A–B). The adopted workflow is presented in detail in Bonali et al. (2019); the photogrammetry processing settings and results are reported in Tables 1 and 2.

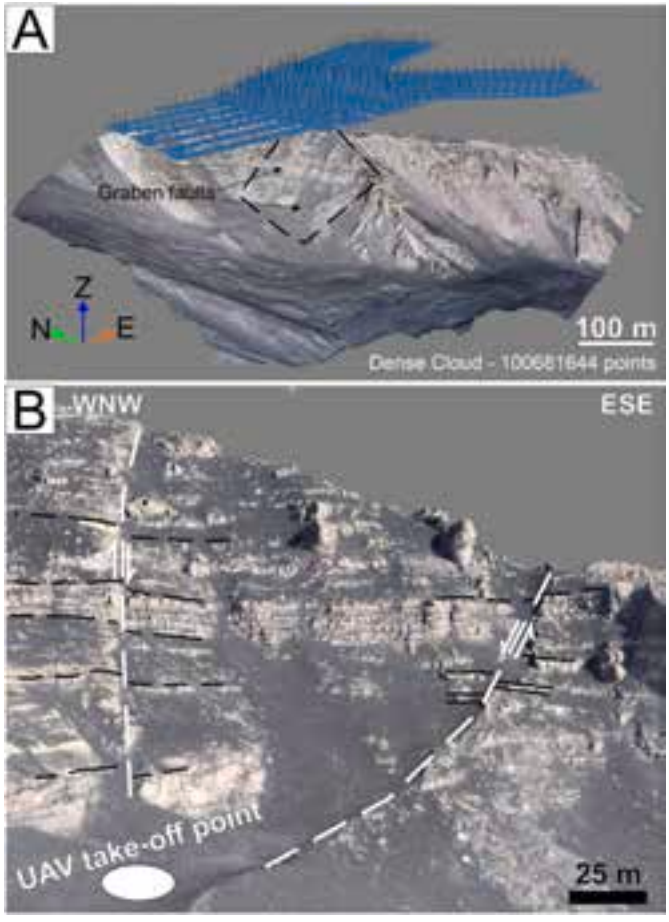

Fig. 4. (A) 3D view of the Dense Cloud and (B) 3D Tiled Model derived from the photogrammetry processing applied to the UAS/UAV-captured images. Black lines highlight marker levels used to calculate the vertical offset along the faults (white dashed lines). Fig. 4B is optimally oriented to highlight the offset layers.

Then, a second survey was conducted in the VdB, with the take-off point at an elevation of about 2130 m a.s.l. (Fig. 4B); its aim was to collect a series of pictures (n = 100) with the camera facing the graben faults, to confirm the observation from 3D inspection. The latter survey was performed with a DJI Mavic 2 Enterprise, allowing for a closer view of the wall.

The DSM and OM were analysed in a GIS environment, whereas the 3D Tiled Model was explored through the Immersive Virtual Reality tool package for photogrammetry-derived models (Gerloni et al., 2018; Tibaldi et al., 2020b; Bonali et al., 2021, 2024). Quantitative data collection was performed using both. The vertical offset was calculated as the difference in elevation between two segments of the same layer, when this was recognized as offset (Fig. 2C–D and 4B). All measurements were related to the coordinate system, including the elevation (m a.s.l.), to analyse variations of the vertical offset and to estimate the average dip of the two graben faults. Finally, several field checks were performed aimed at verifying all the structures affecting the eastern flank down to the easternmost 1971 eruptive vents, during a field activity carried out in the summer of 2022. We collected the height of morphological scarps in the VdB wherever possible, even if this represents a minimum vertical offset in plan view due to the massive recent pyroclastic cover, and we verified the elevation of the referencing of the photogrammetry-derived OM and DSM.

3.3. Numerical modelling

The overall aim of numerical modelling is to investigate the distribution and orientation of stress around the dyke tip, to explore possible relations between the geometry of the graben faults and: *i)* dyke dip depth; *ii)* host rock layering; *iii)* effect of topography. The models were designed with the FEM software COMSOL Multiphysics (v6.1), which allows for the analysis in 2D of the distribution and orientation of dyke-induced stress in an elastic layered medium, considering static modelling. We focused on a key cross-section (Fig. 2A and 5B), which is almost orthogonal to the faults and to the direction of the inferred dyke, where the stratigraphic succession is known (Branca et al., 2011a, Fig. 2B).

We plotted the values of tensile and von Mises shear stresses in the host rock, to investigate their distribution ahead of the dyke tip. Fracturing in the host rock is expected if the tensile stress is at least equal to the *in-situ* tensile strength (T_0) (Gudmundsson, 2011a). For a fault to slip, the von Mises shear stress should be at least equal to the shear strength, that is normally about double the tensile strength (Haimson and Rummel, 1982; Schultz, 1995). In laboratory experiments, tensile strengths of about 5 MPa were obtained for basalts, using intact samples (Graue et al., 2011; Perras and Diederichs, 2014). The *in situ* tensile strengths of rocks obtained by hydraulic fracture experiments are between 0.1 and 9 MPa, with most common values between 2 and 4 MPa (Haimson and Rummel, 1982; Schultz, 1995; Amadei and Stephansson,

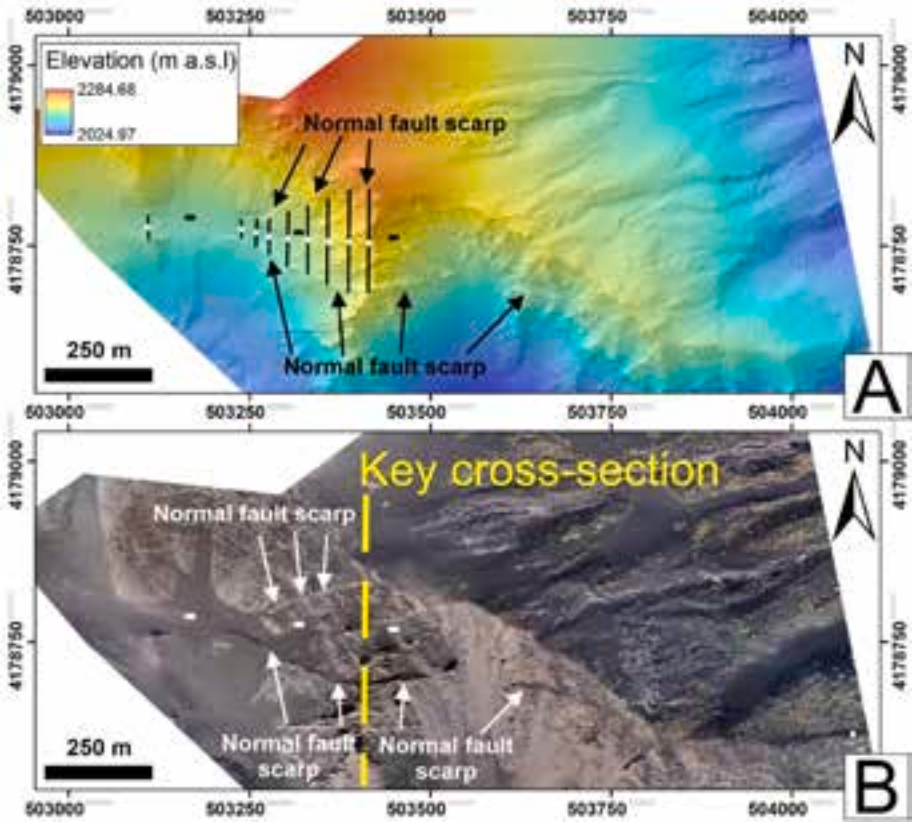

Fig. 5. Photogrammetry-derived (A) DSM (11 cm/pix) and (B) OM (5.5 cm/pix) from UAS-collected pictures, Ref. system: UTM33/WGS84. Black lines in Fig. 5A represent the graben width, the elevation value was collected at their centre (white dots); minus "-" indicates the downthrown block within the graben. Results are shown in Fig. 7B.

Table 1
Summary of settings and results related to the photogrammetry processing.

SfM Photogrammetry processing	Alignment processing settings	High accuracy/Generic and Reference Preselection
	Key Point/Tie Point limit	80000/20000
	Resulting Tie Points	948317
	Dense Cloud processing settings	High Accuracy/Aggressive Filtering
	Resulting Dense Cloud (Points)	100681644
	Resulting DSM Resolution	11 cm/pix
	Resulting Orthomosaic/3D Texture	5.48 cm/pix

1997), which have already been used in previous numerical studies (Al Shehri and Gudmundsson, 2018; Bazargan and Gudmundsson, 2019). In the experiments, the lowest values are assigned to basaltic rock masses weakened (for example) by columnar joints. Since the values of tensile stress that can cause fracturing in the rock can be lower than the most commonly used ones (2–4 MPa), in this work we qualitatively focused our attention on the areas of main concentration of tensile and von Mises shear stresses as favourable for fracturing and faulting, without considering any specific threshold value. A key point in our numerical modelling is to plot the orientation of the greatest compressive stress (σ_1) and the least principal stress (σ_3) as arrows within the host rock, for each of the above listed parameters.

The dyke was modelled as an elliptical cavity with an internal overpressure; we located it at a sufficient distance from the model edges, at the centre of the model along the x-axis, to avoid edge effects (Drymoni et al., 2020, 2023). The overpressure was modelled by defining a normal stress acting on the boundary of the magma body (e.g., Grosfils, 2007). We considered the dyke overpressure constant in all runs and equal to 6 MPa, in agreement with many papers on this topic (e.g. Gudmundsson, 1986, 2011b; Drymoni et al., 2020), also considering that: *i)* the thickness of the 1971 dyke is unknown; *ii)* other dykes cropping out along the northern part of Valle del Bove show a large range of thickness values (about 0.2–5 m) (Ferrari et al., 1991; Scudero et al., 2019).

We modelled the dyke tip at two different depths: Y_1 and Y_2. Y_1 is in agreement with Magee and Jackson (2021), who showed that the dyke tip could be located around the convergence of normal faults at depth, that in our case is at about 2100 m a.s.l. Such depth is 16.5 m deeper

Table 2
Outline of production of DSM and orthomosaic, including the time (in hh:mm:ss) for UAS survey and image collection.

UAS survey/Images Acquisition	**SfM Photogrammetry Processing time**								
	Tie Points		**Depth maps**	**Dense Cloud**	**DSM**	**Orthomosaic**	**3D Tiled Model**	**Total for SfM**	**Overall total**
	Matching	**Alignment**							**Total**
0:30:00	0:40:55	0:31:46	2:51:00	1:52:00	0:00:57	0:14:27	0:51:53	7:02:58	7:32:58

than the one derived applying the so-called dyke rule (Pollard et al., 1983; Mastin and Pollard, 1988). In the flat area at 2130 m a.s.l., in the VdB floor, the graben is characterised by a recognizable width of 27 m; considering this value, the dyke rule would suggest a dyke as deep as 13.5 m. Both depths provided similar results. Therefore, we present results with the tip located at the contact between layers A and B (Y_1), and with the tip located 30 m deeper (Y_2) (Fig. 6). We made this choice to better understand if the depth of the dyke tip have any effects on stress distribution above the dyke, as its relation with the width of the graben is still a debated topic (Trippanera et al., 2015a; Al Shehri and Gudmundsson, 2018; Magee and Jackson, 2021; Drymoni et al., 2023).

We also tested different dip angles for the dyke, considering a pure vertical dyke, and a dyke dipping 75° to the north and to the south (Fig. 6B–D). This is coherent with field data from Ferrari et al. (1991), who suggest that 70% of the dyke intrusions in the northern part of the VdB were emplaced along subvertical planes (also in agreement with Scudero et al., 2019), whereas the remaining 30% were intruded along inclined planes even steeper than 60°. The topographic surface was modelled as a horizontal and 25°-dipping free surface, where no normal or shear stresses are applied (e.g. Apuani et al., 2005; Apuani and Corazzato, 2009; Bistacchi et al., 2012), to explore the modification of the local stress (e.g. Galindo and Gudmundsson, 2012; Becerril et al., 2013). We created two different settings where the upper part of the model represents the topographic surface (Fig. 6): the first with a square box to reproduce a flat topography, and the second with the square box cut in the upper right corner to obtain a free boundary dipping 25° to the south, to better simulate the existing topography (Fig. 2B). The details about the two settings are summarised in Table 3.

First, we created models with a homogeneous host rock for both settings, with E (Young's modulus) = 10 GPa, ν (Poisson's ratio) = 0.25 and ρ (density) = 2600 kg/m^3. Then, for the models with an inclined topography, we tested the role of layering, first with a simplified case with only one mechanical contrast, at a contact located above the tip of the dyke at Y_1 depth (Fig. 6C). We tested four different mechanical contrasts, given by the ratios between E of the upper layer and E of the lower layer: 1/10, 1/4, 4/10 and 10/4, similar to Kavanagh et al. (2006) and Drymoni et al. (2020). Furthermore, in both settings (flat and inclined topography) we tested a layered host rock, as reconstructed from our 3D UAS-derived model with the help of literature data (Branca et al., 2011a), assigning different mechanical properties to different layers.

To calculate the E value of our lava layers, we used the method proposed by Heap et al. (2020), based on the Hoek-Diederichs equation (Hoek and Diederichs, 2006). This equation allows us to obtain the E value of a rock mass starting from the E value of the intact rock (E_i) and using the Geological Strength Index (GSI), a unitless value that describes the rock mass structure (Marinos et al., 2005). To evaluate the GSI, we analysed fracture surface conditions through fieldwork observations, and the rock mass structure thanks to the drone-derived high-resolution 3D model (e.g., Tibaldi et al., 2020b). The resulting GSI values were in the range of 40–55. Therefore, according to the E_i values reported by Heap et al. (2020) for basalts on Mt. Etna and our GSI range, E of the lava layers resulted between 4 and 9 MPa. In our numerical models, we tested E values for lava layers within this range, extending the interval up to 10 MPa, to take into account also the values suggested in the literature by Gudmundsson (2011a) and Drymoni et al. (2023). In this paper, we show only the models that were run with the highest (10 MPa) and the lowest (4 MPa) E values for lava layers, called Set 1 and Set 2, respectively (Table 4).

All the models were fastened at the bottom to avoid rigid-body rotation and translation, putting a fixed constraint in the midpoint of the bottom edge, which was also subjected to a roller boundary condition (Fig. 6A–C). All the models were also subjected to a local extensional stress field of 1 and 3 MPa (F_{ext}), similarly to Drymoni et al. (2023), as the area of our study on Mt. Etna is affected by a predominant extensional regime. This is testified to by: *i)* the presence of normal faults and extension fractures already recognized during field activity (Neri et al., 1991; Tibaldi and Groppelli, 2002; Tibaldi et al., 2022); *ii)* stress inversion with extensional component (Cocina et al., 1997).

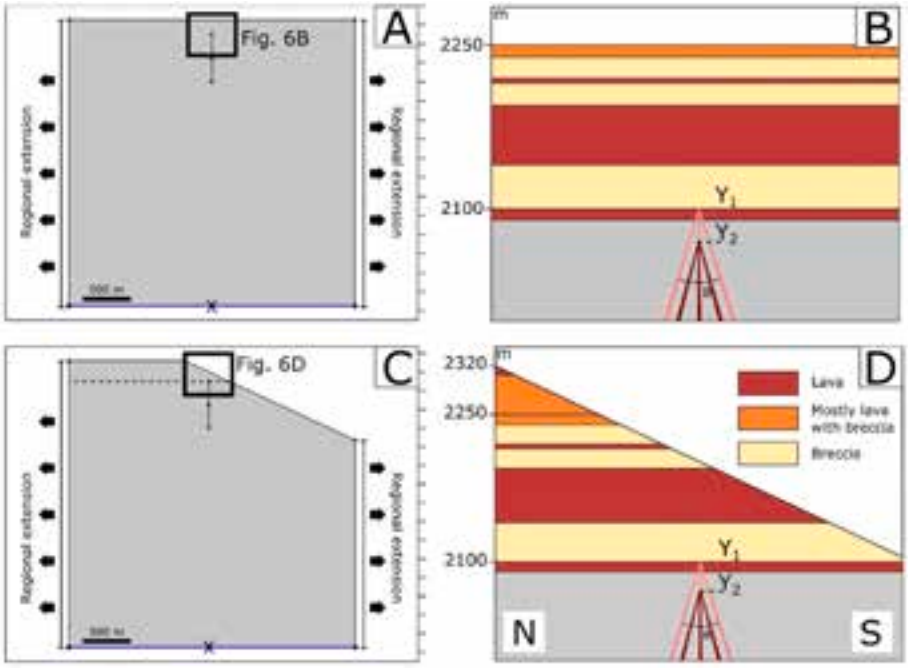

Fig. 6. (A) Numerical model setup to simulate a flat topography. (B) Zoom in the area of interest in case of a flat topography, with the stratigraphy derived from field and literature data (see Fig. 2B). (C) Numerical model setup to simulate a topography with a 25°-dipping slope. The dashed line indicates the location of the contact for the case with a single mechanical contrast. (D) Zoom in the area of interest in case of a 25°-dipping topography, with the stratigraphy derived from field and literature data (see Fig. 2B). In (A) and (C), diverging arrows indicate regional extension. The X symbol at the bottom represents a fixed constraint, whereas the roller boundary condition is indicated in blue. In (B) and (D), the dyke is represented in different colours according to its position (Y_1 or Y_2), and the different dip angles of the dyke are shown. (For interpretation of the references to colour in this figure legend, the reader is referred to the Web version of this article.)

Table 3
Details about the two numerical settings.

	Box dimensions	Triangular meshing size setting	Minimum element quality	Number of boundary triangular elements
Flat topography	3000 x 3000 m	Extremely fine	0.5572 m	42754
25°-dipping topography	3000 x 3000 m	Extremely fine	0.4167 m	40049

Table 4
Mechanical properties of the layers cropping out along the key-section, considered in the numerical modelling. ρ = density of the material, ν = Poisson's ratio, E = Young's modulus; for the latter parameter we used two different sets of values, Set 1 and Set 2.

Layer	ρ (kg/m^3)	ν	Set 1 - E (GPa)	Set 2 - E (GPa)
Lava	2600	0.25	10	4
Breccia	2300	0.25	1	1
Mostly lava with breccia	2500	0.25	7	3
Basement	2600	0.25	10	10

We finally would like to remark that our numerical models are designed with an FEM approach which, to date, has proven to be effective for solving dyke-related processes at the mesoscale (e.g., Browning and Gudmundsson, 2015; Drymoni et al., 2020; Tibaldi et al., 2022) in application to the elastic mismatch criterion (Dundurs, 1969). All the models consider a free surface as upper boundary; therefore, they are not prone to rigid-body translation and no edge effects alter the final stress orientations and magnitude.

4. Results

4.1. Structural data

Comparing the two OMs based on historical photos from 1954 to 1983, we prepared a new structural map of the study area, where the graben can be presently observed (Fig. 7A). The graben structure has a total length of about 2 km and an overall E-W azimuth (Fig. 7), affecting both the floor and the rim of the VdB, as well as part of the eastern flank (Figs. 2–4-5-7). We recognized a total of 13 fault scarps related to dip-slip normal graben faults, two eruptive fissures with a NE-SW strike located along the E flank, and 14 lineaments. The latter are likely the expression of normal faults related to the graben as well, but the vertical offset cannot be nowadays confirmed by field or drone survey due to the present-day pyroclastic coverage that masks the morphological scarps, partially (e.g. Fig. 2B) or totally.

The width of the graben was also quantified on the structural map, and shows an increase with elevation, with values between 27 and 140 m (Fig. 7B). Elevation is in the range 2138–2223 m a.s.l., as can be observed on the UAV-SfM derived DSM (Fig. 5). In Figs. 2–4 it is also possible to notice the geometry of the two graben faults, with the south-dipping fault having an average dip of about 70° and the north-dipping fault having an average dip of 50°. Wherever possible, the vertical offset was quantified (Fig. 4) along specific markers. In fact, in the VdB the height of the morphological scarps is only in the order of a few decimetres, again due to pyroclastic coverage. Differently, along the VdB wall (in section view), vertical offset values were detected (e.g. Fig. 2C–D) and are in the range of 1.9–3.0 m (Table 5). The fault dipping to the south shows values between 2.4 and 3.0 m, the one dipping to the north shows values between 1.9 and 2.8 m. In both cases, the highest values are at the highest elevation. Considering the average dip, the resulting net slip is between 2.6 and 3.2 m (av. = 2.9 m) for the S-dipping fault, and 2.5–3.6 m (av. = 3.0 m) for the N-dipping fault.

With regard to the quality of our dataset, most of quantitative data were collected on photogrammetry-derived models from historical aerial photos and UAS-collected pictures. Historical orthomosaics were referenced with GCPs from referenced topographic maps; structures that are nowadays detectable on satellite images suggest an error close to 1 m. Concerning data collected from UAS-derived 3D models, it has been widely proved that this methodology can be considered reliable and convenient for data collection (e.g. Tibaldi et al., 2020b), with an error

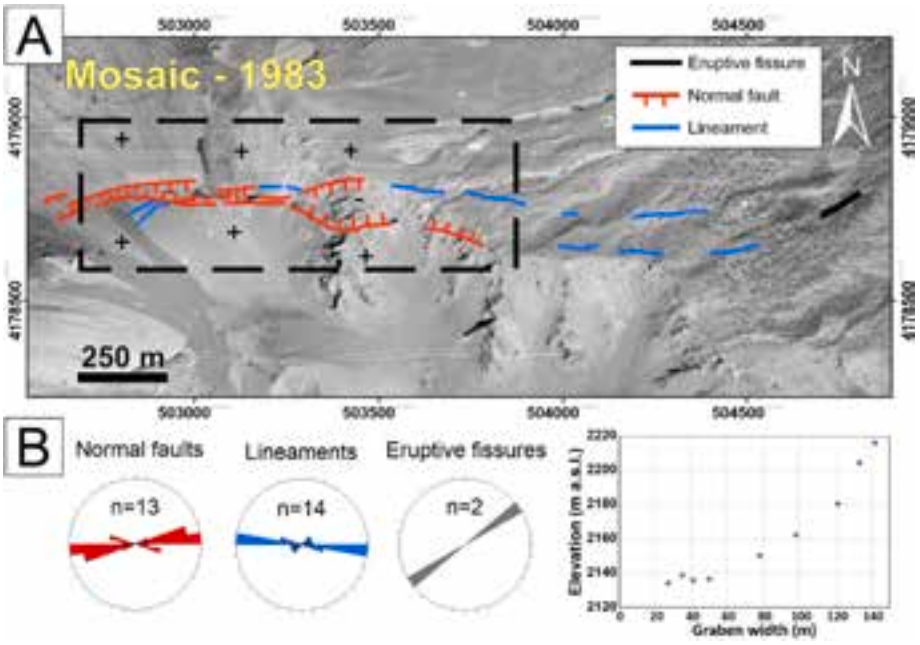

Fig. 7. (A) Mosaic derived from historical aerial photographs (1983). Fault ticks point to the downthrown blocks, that are also highlighted with the symbol '-'. (B) Rose diagrams showing the azimuth of normal faults, lineaments and eruptive fissures formed during the 1971 dyking event, and graph showing the graben width, measured in plan view on the UAS-derived OM, with respect to elevation (centre of the line in Fig. 5). The box shows the area surveyed with drone and field survey.

Table 5
Vertical offset along the two faults, measured on the 3D photogrammetry-derived model from UAV-captured pictures (Fig. 4B). The net slip was calculated using an estimated average dip angle for the two graben faults.

Elevation (m a.s.l.)	Vertical offset (m)	Net slip (m)	Dip dir	Av. Dip Angle (°)
2151	2.5	2.7	South	70
2170	2.8	3.0	South	70
2182	2.4	2.6	South	70
2192	3.0	3.2	South	70
2210	2.7	2.9	South	70
2153	1.9	2.5	North	50
2155	2.9	2.5	North	50
2160	2.8	3.6	North	50
2178	2.6	3.4	North	50

in the scale of centimetres on volcanotectonic structures (Bonali et al., 2019). Additionally, even if the area of this study could have been affected by deformation after 1971, due to the eastern flank instability (Neri et al., 1991, 2004, 2009; Solaro et al., 2010; Siniscalchi et al., 2012; Ruch et al., 2013; Gambino et al., 2022), and the fact that the area between the NE and ENE rifts is the most tectonically active portion of the entire volcanic edifice, there are no evidences that post-1971 faulting occurred. In fact: *i)* field checks carried out in the summer of 2022 did not show any evidence of fault reactivation; *ii)* no sign of fault reactivation over time was observed along the nearby and parallel 1928 fracture system by Tibaldi et al. (2022); *iii)* three offset values measured in the field by one of the authors (MN) in 1990–1991 differ of a few cm from those recently collected; this is equivalent to a difference of 3–4%, which can be considered within the possible measurement error; *iv)* it is reported in the literature that the study area is located within a block that moves homogeneously towards the ESE (details in Bonforte et al., 2011, and references therein); *v)* specifically, interferometry studies conducted on Mt. Etna from the early 1990s onwards confirm that the area of the 1971 fissure is located within a block, as suggested in the previous point (details in Bonforte et al., 2019, and references therein).

4.2. Numerical modelling

4.2.1. Models in a homogeneous host rock

In this section, we present the results of numerical models within a homogeneous host rock. In Fig. 8, we first consider a setting with a flat topography, varying the inclination of the dyke, and with an extensional stress field of 1 MPa. In all cases, both tensile and von Mises shear stresses reach high concentrations from the dyke tip upwards, suggesting likely fracturing and faulting regardless of the dyke attitude. This occurs also when the dyke is not vertical, even if the stresses are distributed asymmetrically, with a greater concentration on one side than the other (Fig. 8B–D).

This asymmetric distribution of stresses is far more evident if we consider a realistic topography along the study key-section, with a slope dipping 25° towards the south (Fig. 9). We observe that the setting with a dyke dipping opposite to the topographic surface is the most favourable to the formation of fractures and faults in the host rock at both sides of the dyke, as observed in the field in the study area (Fig. 9C–F). The setting with a vertical dyke is also, but less, favourable to fracturing and faulting (Fig. 9A–D). On the other hand, the setting with a dyke dipping

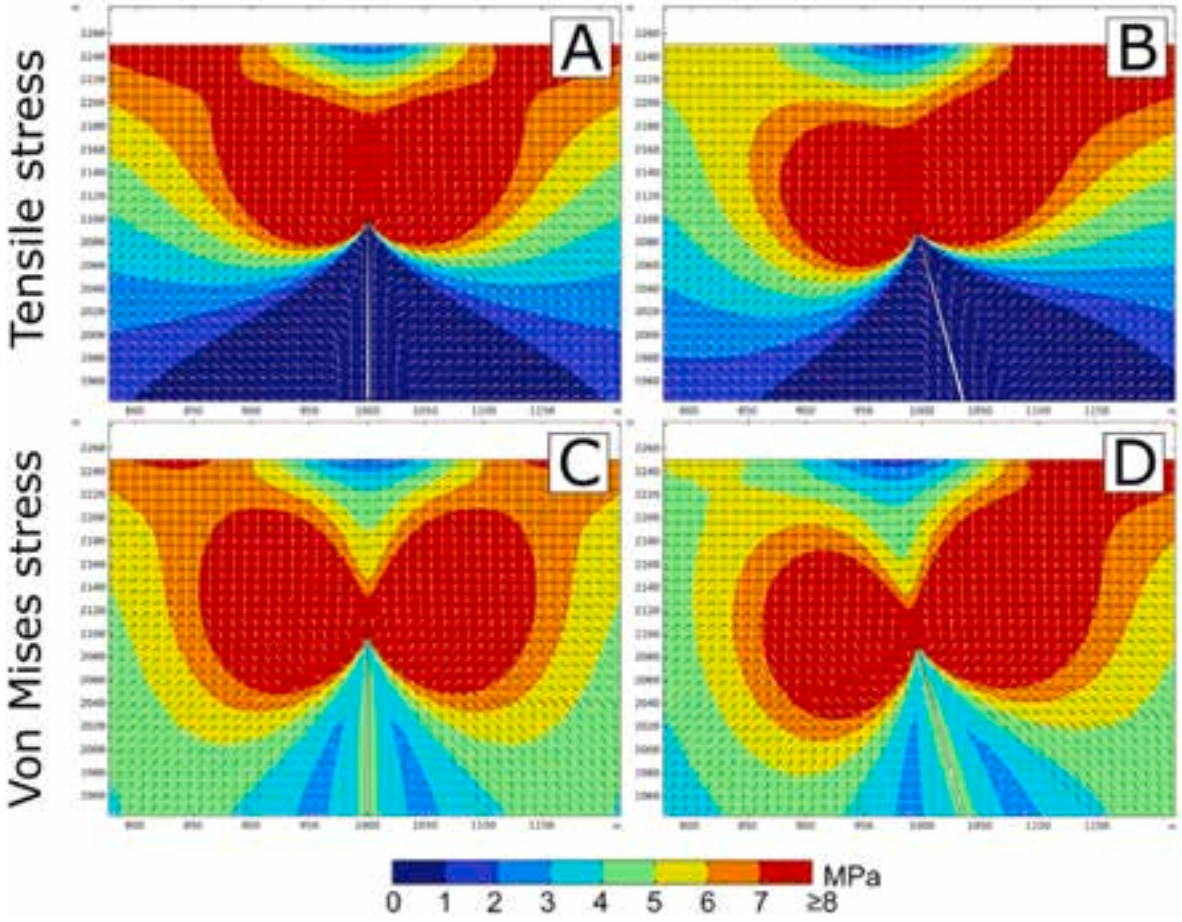

Fig. 8. Numerical models with a homogeneous host rock, a flat topography, extensional stress field of 1 MPa and different dyke attitude. The distributions of tensile (A–B) and von Mises shear (C–D) stresses are shown with the same colour scale bar. Trajectories of σ_1 and σ_3 are shown by white and black arrows, respectively. X and Y axes are expressed in m. (For interpretation of the references to colour in this figure legend, the reader is referred to the Web version of this article.)

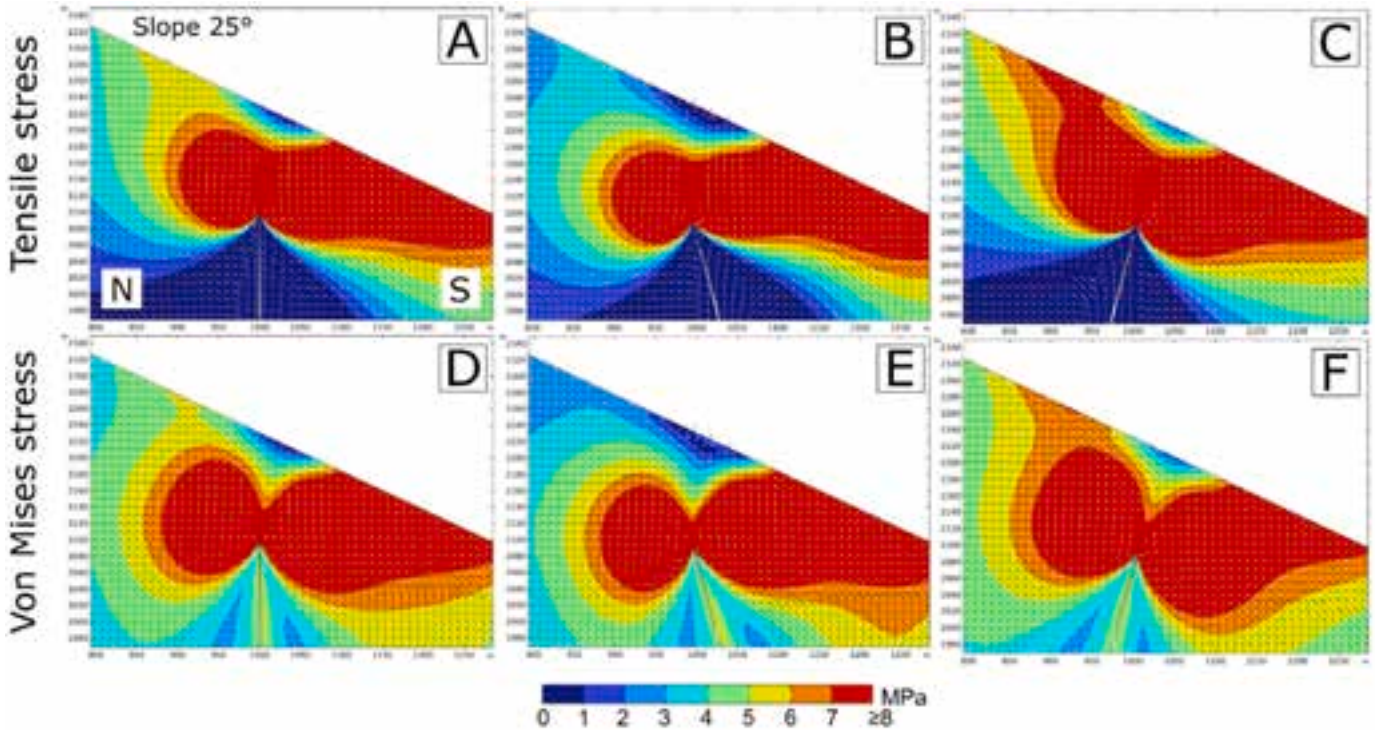

Fig. 9. Numerical models with a homogeneous host rock, and an inclined topography with a slope dipping 25° to the south. The section is oriented N-S. The dyke is modelled with different attitudes under an extensional stress field of 1 MPa. The distributions of tensile (A-B-C) and von Mises shear (D-E-F) stresses are shown with the colour scale bar. Trajectories of σ_1 and σ_3 are shown by white and black arrows, respectively. X and Y axes are expressed in m. Y represents the elevation a.s.l. (For interpretation of the references to colour in this figure legend, the reader is referred to the Web version of this article.)

to the south, in the same direction of the topographic surface, is the least consistent with what was observed in the field, because the von Mises shear stress distribution is favourable to the formation of just one fault to the south (Fig. 9E). Additionally, with the inclined topography, we notice a strong clockwise rotation of σ_1 and σ_3 orientation in the host rock that does not change significantly with the inclination of the dyke.

4.2.2. *Models with realistic layering and flat topography*

In this set of models, we introduce the stratigraphy that was observed in the field along our key-section (Fig. 2B), with a flat topography. Regarding the mechanical properties of the layers, we show two main sets (Set 1, Set 2) of models, as shown in Table 4. The dyke is modelled with two different attitudes and with an extensional boundary of 1 and 3 MPa, also considering two different depths for the dyke tip (details for depth Y_2 are always shown in the Supplementary materials).

If we consider an extension of 1 MPa, in all the models, the tensile stress is mostly concentrated in lava layers and mostly suppressed in breccia layers. When the dyke is vertical, the stress distribution is symmetric above the dyke tip, whereas it becomes asymmetric when the dyke is inclined. In the first case, we notice that the most favourable setting for fracturing, above the dyke tip, is in all lava layers (Fig. 10A–C). Differently, when the dyke is inclined, one side shows an area with a more favourable setting for fracturing than the other side (Fig. 10B–D). Increasing the extensional strain to 3 MPa, the distribution of tensile stress is the same, but the magnitude increases both in lava and in softer layers (Fig. 10I-J-K-L). Tensile stress is generally higher at the dyke tip at depth Y_1, with respect to the greater depth Y_2.

If we consider the von Mises shear stress distribution in Set 1 with an extension of 1 MPa, we generally notice a high concentration in the first level of breccia and generally in all lava layers, whereas it decreases in the two uppermost breccia layers (Fig. 10E–F). As observed for the tensile stress, stress distribution is symmetric with the vertical dyke (Fig. 10E), whereas it becomes asymmetric when the dyke is inclined (Fig. 10F). Regarding σ_1 and σ_3 orientation, they become asymmetric when the dyke is inclined and rotate only on one side. Generally, increasing the extensional strain, the magnitude of the von Mises shear stress increases in the layers (Fig. 10M–N), whereas the orientation of σ_1 and σ_3 is not affected by this parameter. Deepening the dyke tip to Y_2, the von Mises shear stress magnitude generally decreases. Regarding Set 2 (Fig. 10C-D-G-H-K-L-O-P), we notice that the main differences with respect to Set 1 pertain to the magnitude of both the tensile and von Mises shear stresses. Indeed, stress distribution is more homogeneous among the layers, with lower magnitude in lava layers and a higher magnitude in breccia layers with respect to Set 1. Observations about the setting that is more, or less, favourable for fracturing and faulting are generally the same as Set 1, as well as the results regarding the orientation of σ_1 and σ_3.

4.2.3. *Models with realistic layering and topography*

In this set of models, we introduce layering with a topographic surface dipping 25° to the south. First, we modelled a simplified case, with a single mechanical contrast at a contact located above the tip of the dyke, at depth Y_1 (Fig. 6C). In these models (run with contrasts of 1/10, 1/4, 4/10 and 10/4), we observe that the difference of E between the layers affects tensile and von Mises shear stress distributions, that concentrate in the stiffer layers, whereas no relevant effects are observed regarding σ_1 and σ_3 orientation (see the Supplementary materials for details). Then, we introduced in the models the stratigraphy that we observed in the field along our key-section (Fig. 6D). Also in this case, we show two main sets of models, Set 1 and Set 2 (Table 4). The dyke is modelled with different attitudes and with an extensional boundary of 1 and 3 MPa, considering two different depths for the dyke tip (details for depth Y_2 are shown in the Supplementary materials).

Regarding Set 1, tensile stress is mostly concentrated in lava layers, followed by mostly lava layers, with stress suppression in breccia layers. Considering the geometry, when the dyke is dipping to the north, opposite to the topographic surface, we notice the most favourable setting for fracturing at both sides of the dyke, with tensile stress that

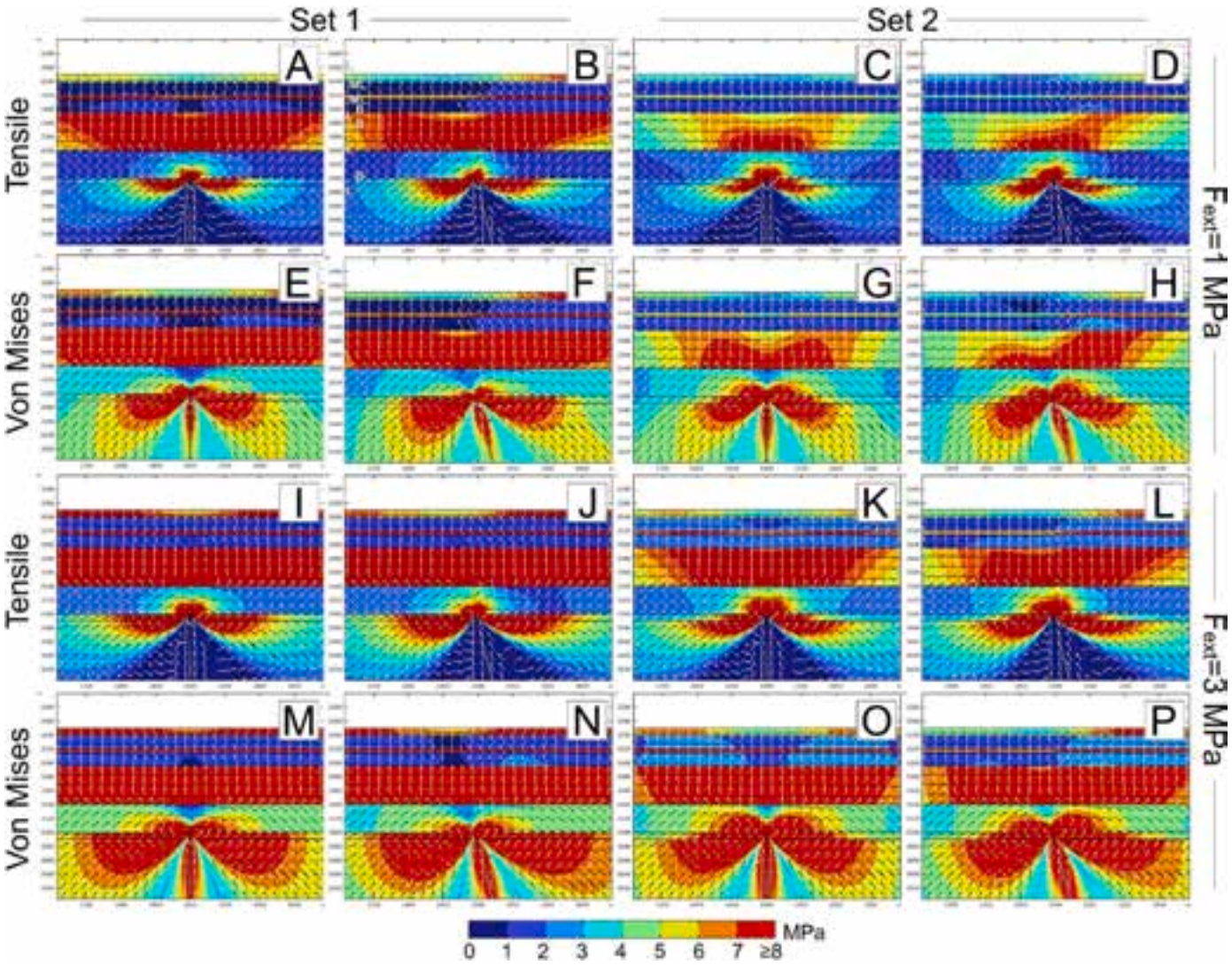

Fig. 10. Numerical models with layering based on field observations and with E values from Set 1 and Set 2 (Table 4). The different layers are the same as in Fig. 6 (B = Breccia, ML = Mostly lava with breccia, L = Lava, as indicated in Fig. 10B). Dyke is modelled with different attitudes, as well as taking into account extensional stress fields of 1 and 3 MPa. The distributions of tensile (A-B-C-D-I–J-K-L) and von Mises shear (E-F-G-H-M-N-O-P) stresses are shown with the colour scale bar. Trajectories of σ_1 and σ_3 are shown by white and black arrows, respectively. X and Y axes are expressed in m. (For interpretation of the references to colour in this figure legend, the reader is referred to the Web version of this article.)

distributes up to the uppermost layers with higher concentrations, followed by the setting with the vertical dyke. The setting with the dyke dipping to the south, in the same direction as the topographic surface, shows the least favourable configuration for fracturing at both sides of the dyke, because high concentrations of tensile stress are reached just at the southern side. This is observed for both settings with 1 MPa (Fig. 11A-B-C) and 3 MPa (Fig. 11G-H-I) of extensional boundary. Increasing the extensional strain, the magnitude of tensile stress increases.

If we take into account the von Mises shear stress distribution in the layers above the dyke tip, we generally notice a high concentration in the first level of breccia and in the upper lava, then a decrease in the upper breccia layers, a high concentration in the thinner upper lava level and a higher concentration in the uppermost layers compared to the breccia levels below (Fig. 11D-E-F). The highest concentration of the von Mises shear stress in the area, consistent with the two faults visible in the field, is observed when the dyke dips to the north, opposite to the topographic surface, followed by the vertical dyke. The setting with the dyke dipping to the south, in the same direction as the slope, shows the least favourable configuration to faulting at both sides of the dyke. This pattern is observed for both the setting with 1 MPa (Fig. 11D-E-F) and 3 MPa (Fig. 11J-K-L) of extensional boundary. Increasing the extensional strain, the magnitude of the von Mises shear stress increases. Considering the orientation of σ_1 and σ_3, we notice that in all scenarios there is a general clockwise rotation of both, from the lava layer up to the uppermost layers along the key-section. The orientation does not show relevant changes with the increase of the superimposed extensional regime.

Regarding Set 2 (Fig. 12), the main differences with respect to Set 1 regard the magnitude of both tensile and von Mises shear stresses, as noticed for the setting with a flat topography. The distribution of stresses is more homogeneous among the layers, with lower magnitude in lava layers and a higher magnitude in breccia layers compared to Set 1. Observations about the setting that is favourable for fracturing and faulting are generally the same as Set 1, as well as the orientation of σ_1 and σ_3. Finally, increasing the depth of the dyke tip (Y2) in the numerical modelling, the result is that the von Mises shear stress magnitude generally decreases.

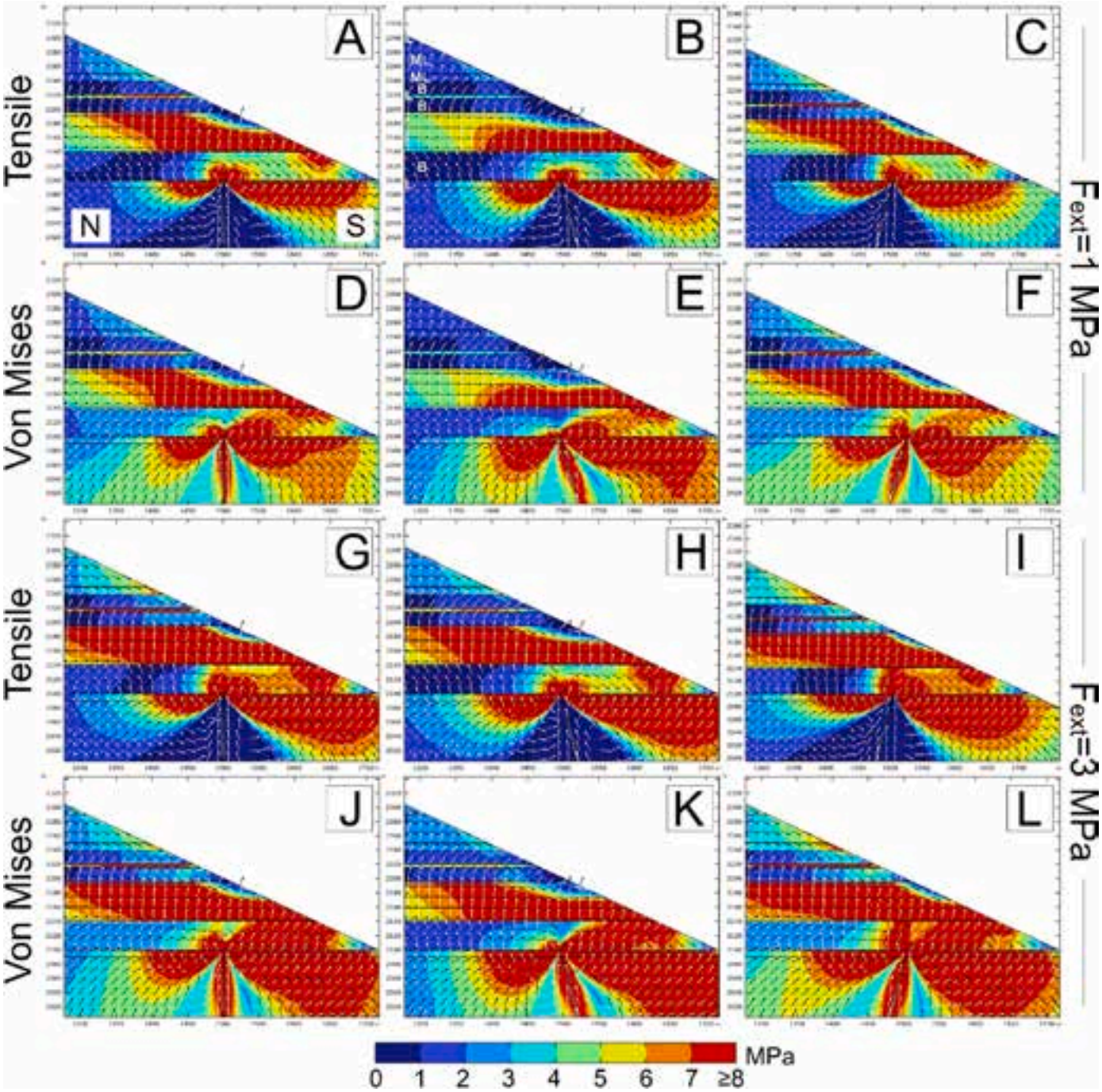

Fig. 11. Numerical models with layering and topography based on field observation, E values are from Set 1 (Table 4); the section is oriented N-S. The different layers are the same as in Fig. 6 (B = Breccia, ML = Mostly lava with breccia, L = Lava, as indicated in Fig. 11B). The dyke is modelled with different attitudes, as well as taking into account extensional stress fields of 1 and 3 MPa. The distribution of tensile (A-B-C-G-H-I) and von Mises shear (D-E-F-J-K-L) stresses is shown with the colour scale bar. Trajectories of σ_1 and σ_3 are shown by white and black arrows, respectively. X and Y axes are expressed in m. Y represents the elevation a.s.l. (For interpretation of the references to colour in this figure legend, the reader is referred to the Web version of this article.)

5. Discussion

5.1. Graben geometry and magnitude of the deformation

Normal fault scarps and lineaments show an overall E-W direction (Fig. 7) with a slight rotation to ENE at the easternmost part, where the eruption took place on the eastern flank of the volcanic edifice. The length of the area affected by faulting is in the 1–2 km range: the lower value includes only the total length of the structural elements classified as normal faults, and the greater value considers also the length of the lineaments. Although this length is not within the range given by the classical empirical relationship between magnitude and the fracture length for normal faults (Wells and Coppersmith, 1994; Blaser et al., 2010), this kind of faulting certainly produced earthquakes during graben development (e.g. Bonaccorso et al., 2011; Ruch et al., 2016; Fischer et al., 2022), with M lower than 4.5, based on the minimum value provided by Blaser et al. (2010).

With regard to the relationship between the depth of the dyke tip and the width of the graben (e.g., Mastin and Pollard, 1988; Trippanera et al., 2015a), our case study, where the faults are very well exposed, is

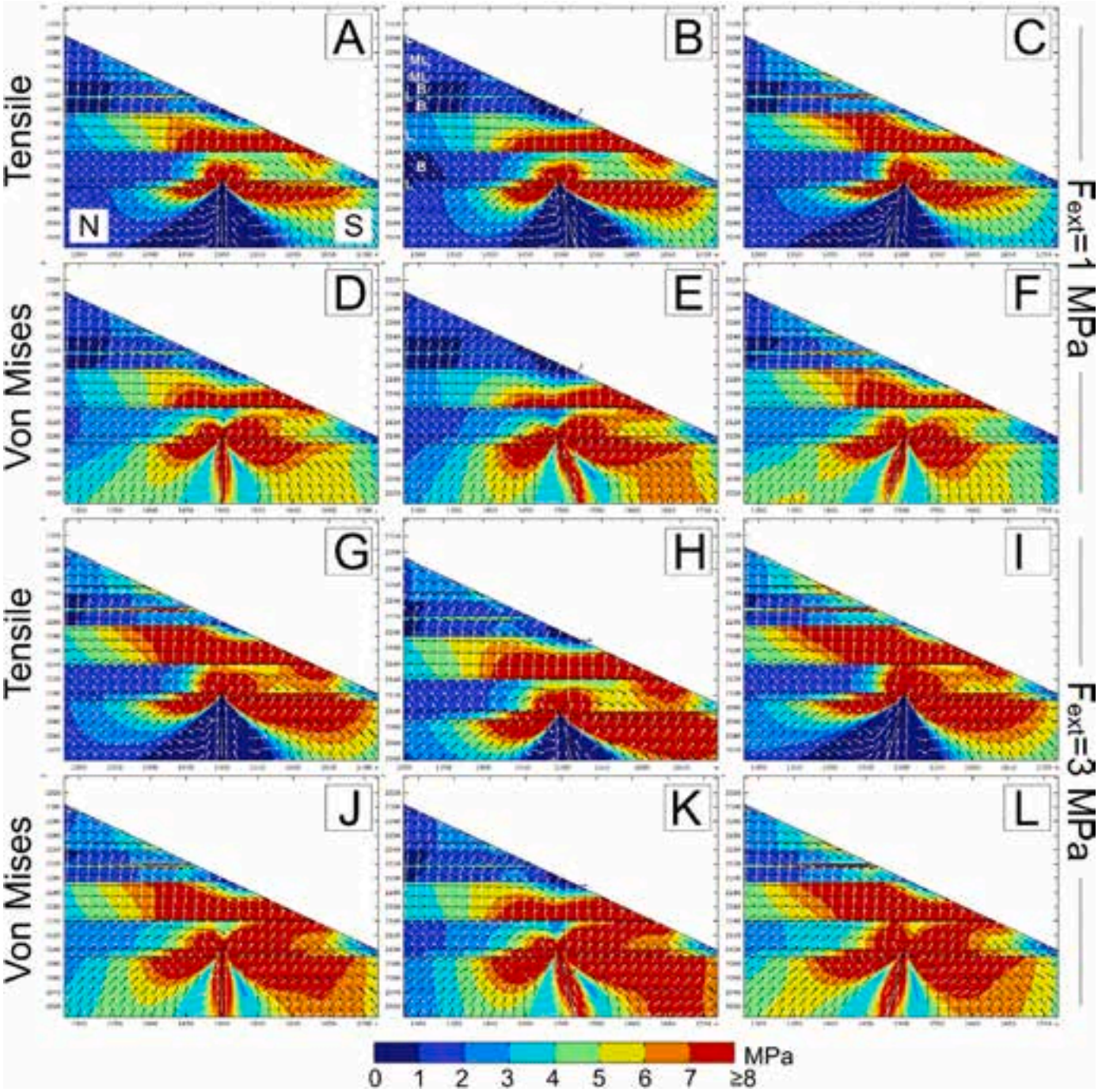

Fig. 12. Numerical models with layering and topography based on field observation, E values are from Set 2 (Table 4); the section is oriented N-S. The different layers are the same as in Fig. 6 (B = Breccia, ML = Mostly lava with breccia, L = Lava, as indicated in Fig. 12B). Dyke is modelled with different attitudes, as well as taking into account extensional stress fields of 1 and 3 MPa. The distributions of tensile (A-B-C-G-H-I) and von Mises shear (D-E-F-J-K-L) stresses are shown with the colour scale bar. Trajectories of σ_1 and σ_3 are shown by white and black arrows, respectively. X and Y axes are expressed in m. Y represents the elevation a.s.l. (For interpretation of the references to colour in this figure legend, the reader is referred to the Web version of this article.)

consistent with Magee and Jackson (2021), who show through geophysical data that the tip of the dyke could be located around the convergence of normal faults at depth. Conversely, we do not agree with the so-called "dyke rule", derived from Pollard et al. (1983) and widely used in the literature (e.g. Rubin, 1992; Hjartardóttir et al., 2016; Al Shehri and Gudmundsson, 2018), which suggests that dyke-induced grabens have a width roughly equal to twice the depth of the dyke top. If we applied this rule to our case study, this would imply that for a graben width of 27 m to the west, and 143 m to the east, the dyke tip would be at a depth of 13.5 m and 71.5 m, respectively. Considering the difference in height of 82 m, this results in an elevation range for the dyke tip of 2125–2150 m a.s.l., within a horizontal distance of about 500 m (Fig. 5A). This implies a dyke propagation of 500 m eastward and 25–30 m upward; instead, the location of the latest 1971 eruptive vents suggests an overall eastward and downward propagation of the dyke tip from the uppermost vents, to the west, to the lowermost to the east (inset of Fig. 1).

Vertical offsets show that the highest values are found at the highest elevation, and that subsidence was of about 2.5–3 m at the surface. This value is in agreement with the Afar 2005 event that caused a subsidence

of 2–3 m in the northern rift segment, even if the tip of the dyke was inferred at a depth of 2 km (Wright et al., 2006). However, it is lower than the maximum vertical displacement of 6 m observed by Ruch et al. (2016) during the Bardarbunga dyke propagation, where the depth of the dyke tip was hypothesised at 300–400 m (Hjartardóttir et al., 2016; Ruch et al., 2016). Trippanera et al. (2019) measured a vertical offset up to 3 m along dyke-induced normal faults in Harrat Lunayyir (Saudi Arabia) by using high-resolution drone imagery. In this case, the top of the intrusion was given at a depth of 1–2 km below the surface (Pallister et al., 2010; Xu et al., 2016). Along the same ENE rift zone on Mt Etna, Tibaldi et al. (2022) quantified the surface deformation occurred during the 1928 fissure eruption, detecting graben faults in plan view (and not in section). The graben is wider in the western and uppermost part, while a narrow graben is observed in the easternmost and lower part of the surveyed area, with an average vertical offset of 2.4 and 1.1 m, respectively. A series of eruptive vents were identified in the middle of the uppermost graben, showing that the dyke propagated up to the surface, whereas no eruptive vents are present in the easternmost part. However, here the dyke is supposed to be very shallow, about 12 m below the surface, even if its precise depth is still undefined. Our work on the 1971 event thus contributes to the discussion on dyke-induced subsidence/faulting, with new constraints for shallower depths of the dyke tip, even if its thickness was not defined. Differently, our values of vertical offset are greater than what expected if we consider the length–displacement scaling factor proposed for co-seismic rupture in volcanic regions by Gudmundsson et al. (2013). Additionally, our data also show that the studied graben is asymmetric with regard to the inclination of the two bounding normal faults. The south-dipping plane's inclination is 70° and the north-dipping fault plane's inclination is 50°. This asymmetry would have been undetected with classical plan-view studies (Sigurdsson, 1980; Gudmundsson and Bäckström, 1991; Rubin, 1992; Acocella and Neri, 2003; Billi et al., 2003; Ebinger et al., 2010; Pallister et al., 2010; Bonaccorso et al., 2011; Trippanera et al., 2015b, 2019; Acocella and Trippanera, 2016; Hjartardóttir et al., 2016; Ruch et al., 2016; Al Shehri and Gudmundsson, 2018; Tibaldi et al., 2020a), as the vertical offsets for the two faults show similar values (Table 5).

5.2. *Dyke-induced stresses, topography and graben fault geometry*

The formation of normal faults and grabens was observed in Iceland during historical dyking episodes, like the 1975–1984 Krafla Fires (Sigurdsson, 1980; Rubin, 1992) and the 2014 Bardarbunga episode (Sigmundsson et al., 2015; Hjartardóttir et al., 2016; Ruch et al., 2016), as well as on Mt. Etna, associated with the events of dyke propagation in 1809 (Geshi and Neri, 2014), 1928 (Tibaldi et al., 2022), 1983 (Murray

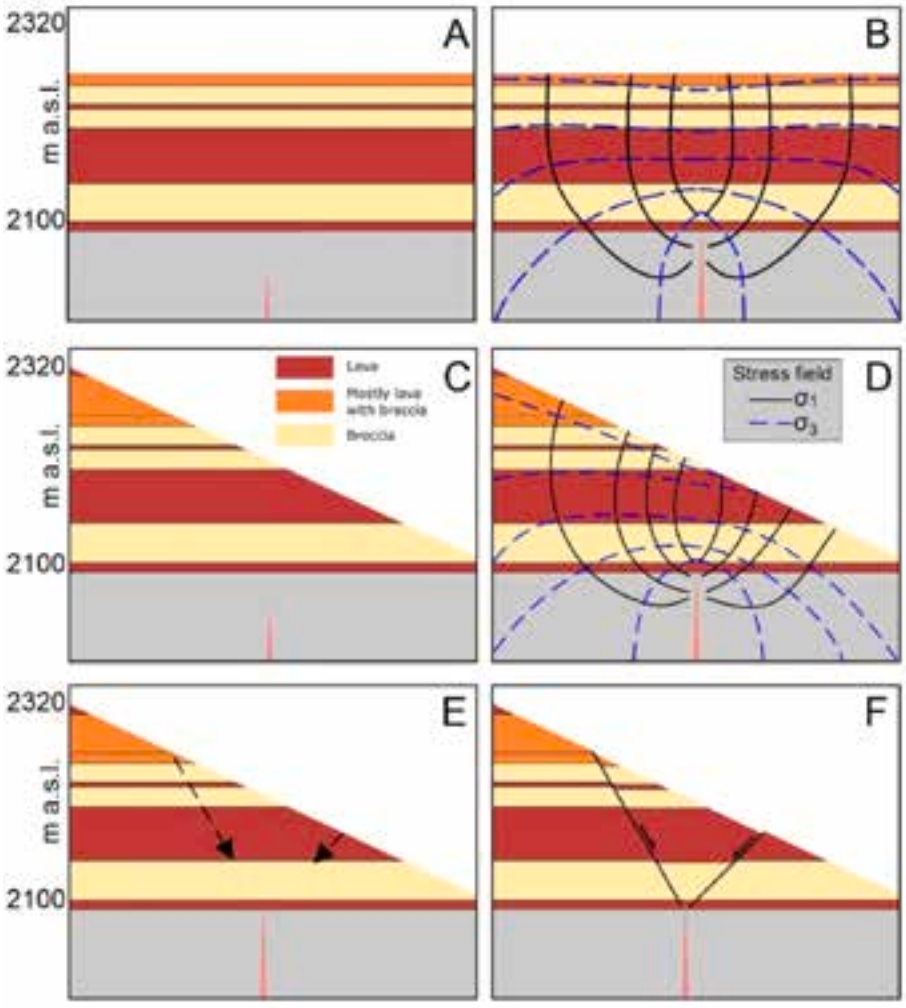

Fig. 13. Scheme aimed at summarising the process of graben faults formation, according to our results. (A–B) The dyke intrudes in a layered host rock volume, characterized by a flat topographic surface. (C–D) The dyke intrudes in a layered host rock volume, characterized by an inclined topographic surface. The orientation of σ_1 and σ_3 rotates clockwise, due to the inclined topography, causing an asymmetry of the dyke-induced stress field. (E) Faults start nucleating at the surface and propagate downward. (F) Two inward-dipping normal faults develop and create a graben, with an asymmetric geometry.

and Pullen, 1984), 2001 (Acocella and Neri, 2003), 2002–2003 (Neri et al., 2004), 2004–2005 (Neri and Acocella, 2006), 2008 (Bonaccorso et al., 2011), 2013 (Falsaperla and Neri, 2015) and 2018 (Calvari et al., 2020). We integrate this topic with a new aspect, showing asymmetric dip angles for the two graben faults (Fig. 2A). Understanding which parameters contributed to this geometrical fault setting was the main topic of the modelling, which focused on the relation between dyke-induced stresses in the host-rock and the deformation observed in section view (Figs. 2 and 4). Furthermore, we paid attention to the conditions that can promote both fracturing and faulting, in terms of variations of tensile and von Mises shear stress concentration induced by dyke overpressure (e.g. Al Shehri and Gudmundsson, 2018; Bazargan and Gudmundsson, 2019; Drymoni et al., 2023).

Our models suggest that the main parameter controlling the observed graben fault geometry is the topography, especially in terms of σ_1 and σ_3 orientations (Fig. 13). If we consider the classical likelihood-arrangement for a fault plane with respect to σ_1 and σ_3 orientations (e.g. Anderson, 1905; Hafner, 1951; Ramsay and Lisle, 2000; Fossen, 2016), we observe that: *i)* varying stiffness values of the lava layers does not affect σ_1 and σ_3 orientation in the host-rock; *ii)* a different dyke inclination, with horizontal topography, results in an asymmetric setting for σ_1 and σ_3, promoting an asymmetric likelihood-arrangement for the graben faults; however, this arrangement is not similar to that observed in the field; *iii)* the topography with an inclination of 25° always causes a clockwise rotation of σ_1 and σ_3, regardless of dyke attitude, depth and layering of the host rock. The latter considerations suggest a key role of topography in dictating σ_1 and σ_3 rotation (Fig. 13C–D), which promotes the fault attitude observed in the field along the key-section (Fig. 4B). The effect of topography on dyke-induced surface deformation was already observed through analogue models, for example by Trippanera et al. (2015a), who showed that the presence of a relief can also affect the width of the graben. However, these authors considered the graben in plan view, without focusing on the geometry of the underlying faults, differently from our case study.

With regard to tensile and von Mises shear stresses distributions, in the case of an inclined south-dipping topography (Fig. 9), results show that the most favourable conditions for fracturing and faulting are found with a vertical dyke or with a dyke that dips opposite to the topographic surface. As observed in the literature (Al Shehri and Gudmundsson, 2018; Bazargan and Gudmundsson, 2019), soft layers have the capability of suppressing both tensile and von Mises shear stress (e.g. Fig. 10).

Additionally, we suggest that the propagation of the 1971 dyke was guided by the large-scale topography of the volcano, linked to unbuttressing due to the presence of the VdB depression. Our structural data clearly show that the 1971 swarm of fissures and faults cuts the VdB bottom and then intersects obliquely its lateral escarpment (Fig. 7A). More to the east, above the shoulder of the VdB, the swarm runs exactly parallel to the VdB escarpment, i.e. with an E-W trend. This orientation of the fracture swarm should be the effect of the underlying dyke trend, which here propagated parallel to the VdB scarp. This attitude was already observed at Stromboli volcano, where several dykes that developed after the formation of the Sciara del Fuoco lateral collapse amphitheatre followed the collapse scarps (Tibaldi, 1996, 2001, 2003, 2004; Neri et al., 2008; Neri and Lanzafame, 2009), and at Somma-Vesuvio, where the buttress of Mt. Somma hinders the propagation of the shallow radial dikes towards the north (Acocella et al., 2006, 2009). A similar behaviour was recognized also at Ollagüe volcano, Chile (Vezzoli et al., 2008), and was demonstrated by analogue modelling (Acocella and Tibaldi, 2005).

5.3. Graben fault nucleation

Another debated topic concerning dyke-induced faulting regards the nucleation of graben faults. In the last decades, this topic has been investigated mainly by analogue modelling. Mastin and Pollard (1988) observed first the formation of vertical fractures around the top of the dyke, and then at the surface, that subsequently connect within each other developing the graben. Trippanera et al. (2015a) carried out experiments with a similar setting but simulating different depths (100–800 m in nature) and intrusion shapes, with rectangular and triangular intrusive complexes. In all their models, the throw of normal faults is higher at the surface and decreases downward. Regarding graben fault geometry, we focused our attention on experimental results by Trippanera et al. (2015a) for a scaled depth of 100–200 m, where it is shown that the faults have an inward-dipping geometry and are geometrically connected to the dyke tip. Additionally, Trippanera et al. (2015a) calculated the 2D Coulomb stress change on optimally oriented faults due to a vertical opening fracture, showing that normal faulting is enhanced at the surface to the sides of the dyke. Therefore, they concluded that the dyke-induced steeply-dipping normal faults nucleate close to the surface and propagate downward, in agreement with Gudmundsson and Bäckström (1991), Forslund and Gudmundsson (1992) and Acocella et al. (2003). This result is also coherent with numerical models by Gudmundsson (1998), who showed that caldera faults would commonly nucleate from tension fractures at the surface, and then develop to normal faults at depth. Our field data also show that vertical offset values are slightly greater at higher elevation along both faults of the graben (Table 5), suggesting a downward propagation of the graben faults (Fig. 13C–D).

Other authors, instead, support the hypothesis of an upward propagation of dyke-induced faults, from depth to the surface, based on field observations and numerical models of faults in Iceland (Grant and Kattenhorn, 2004; Tentler, 2005), but they do not provide quantitative data in section view for a proper comparison with our case study. More recently, Rivas-Dorado et al. (2023) proposed a hybrid model of dyke-induced fault nucleation, using analytical modelling applied on three grabens on Mars. They suggest that in case of shallow narrow dykes, nucleation occurs through linkage of mode I cracks that form near the surface and mode II discontinuities that are generated near the tip of the dyke. The simultaneous formation of downward moving tensile fractures at the surface and of upward moving inwards shear fractures was suggested also by Folch and Martı (2004) for large plate-subsidence calderas.

If we take into account the results of our numerical models, we notice that dyking is capable of inducing a greater increase in both tensile and von Mises stresses in stiffer lavas, compared to softer breccia layers, consistently with the results by previous authors (Gudmundsson, 2003; Philipp et al., 2013; Tibaldi et al., 2022; Corti et al., 2023; Drymoni et al., 2023). According to our models, the formation of two faults, coherently with field observations, is expected in the case of a vertical dyke or of a N-dipping dyke. If we consider these cases, we notice that the N-dipping fault could nucleate both in the surface lava layers, characterised by high values of tensile and von Mises stresses, and at the dyke tip (Figs. 11–12). However, our structural data suggest that fault nucleation occurred at the surface and then propagated downward. Regarding the S-dipping fault, in the models we observe a greater increase of stresses at the tip of the dyke and in the uppermost lava layer, whereas the values increase, but reaching lower values, at the surface layers (mostly lavas with breccias) (Figs. 11–12). Therefore, the increase of stresses at the surface could still support a downward propagation of the faults, but it cannot exclude the hypothesis of a hybrid fault nucleation (with mode I cracks that form near the surface and mode II cracks that generate at the tip of the dyke), as proposed by Rivas-Dorado et al. (2023). However, considering also our field-collected structural data, we support the model proposed by Trippanera et al. (2015a), suggesting a fault nucleation at the surface and a downward propagation.

6. Conclusions

In this study, we analysed a unique example of dyke-induced surface deformation associated with the 1971 eruptive event on the eastern

flank of Mt. Etna, where the graben faults are shown both in section and plan view. Integrating data from fieldwork and photogrammetry-derived models, we characterised the lithostratigraphy of the rock succession and the deformation along the graben faults, measuring the graben width, the fault attitudes and the vertical offsets, with the following results: *i)* the studied graben is asymmetric in terms of the attitude of the faults, with one fault that dips 70° to the south, and the other one that dips 50° to the north; *ii)* values of vertical offset in section view are greater in the uppermost part and decrease downward; *iii)* fracture field geometry and orientation related to the 1971 dyke support the hypothesis that its propagation could have been affected by the large-scale topography of the volcano, as reported in the literature for other volcanoes; *iv)* the depth of the dyke tip is expected to be located around the convergence of normal faults at depth.

The comparison between field data and numerical models suggests a few additional and relevant findings: *i)* the inclined topography played a key role, as shown in section view, in determining the orientation of dyke-induced σ_1 and σ_3 in the host rock that, in turn, controls the geometry of graben faults resulting in such an asymmetric setting; *ii)* dyke-induced stress concentrations and vertical offset values support the hypothesis of a downward propagation of the graben faults, from the surface down to the dyke tip.

CRediT authorship contribution statement

Fabio L. Bonali: Writing – original draft, Supervision, Methodology, Investigation, Conceptualization. **Noemi Corti:** Writing – original draft, Methodology, Investigation. **Federico Pasquaré Mariotto:** Writing – original draft, Investigation. **Emanuela De Beni:** Writing – original draft, Methodology, Investigation. **Sofia Bressan:** Investigation. **Massimo Cantarero:** Methodology, Investigation. **Elena Russo:** Writing – review & editing, Investigation. **Marco Neri:** Writing – original draft, Investigation. **Alessandro Tibaldi:** Writing – original draft, Supervision.

Declaration of competing interest

The authors declare that they have no known competing financial interests or personal relationships that could have appeared to influence the work reported in this paper.

Data availability

Data will be made available on request.

Acknowledgments

We thank the editor Toru Takeshita and two anonymous reviewers for their comments, which helped us improve our manuscript. This work was carried out under the framework of the CRUST - Interuniversity Centre for 3D Seismotectonics with Territorial Applications, and under the aegis of the International Lithosphere Program, Task Force II. This paper is also an outcome of the Virtual Reality lab for Earth Sciences - GeoVires (https://geovires.unimib.it/), University of Milano-Bicocca. Agisoft Metashape is acknowledged for photogrammetry processing. Our work was also supported by funding from the convention "All. A INGV-DPC" and by PRL 2019 Developing a semi-automatic method for data collection and volcanic hazard assessment in volcano failure prone areas using UAV-derived dense clouds. This paper does not necessarily represent DPC official opinion and policies. We acknowledge the "Parco dell'Etna" (https://parcoetna.it/) for permission to perform the survey. We would like to thank Daniele Pennisi and Francesco Ciancitto for helping us on the way up and down the Valle del Bove.

Appendix A. Supplementary data

Supplementary data to this article can be found online at https://doi.org/10.1016/j.jsg.2024.105231.

References

Acocella, V., Neri, M., 2003. What makes flank eruptions? The 2001 Etna eruption and its possible triggering mechanisms. Bull. Volcanol. 65, 517–529.
Acocella, V., Tibaldi, A., 2005. Dike propagation driven by volcano collapse: a general model tested at Stromboli, Italy. Geophys. Res. Lett. 32 (8).
Acocella, V., Neri, M., 2009. Dike propagation in volcanic edifices: overview and possible developments, Special Issue: Gudmundsson – Volcanoes. Tectonophysics 471, 67–77. https://doi.org/10.1016/j.tecto.2008.10.002.
Acocella, V., Trippanera, D., 2016. How diking affects the tectonomagmatic evolution of slow spreading plate boundaries: overview and model. Geosphere 12 (3), 867–883.
Acocella, V., Korme, T., Salvini, F., 2003. Formation of normal faults along the axial zone of the Ethiopian Rift. J. Struct. Geol. 25 (4), 503–513.
Acocella, V., Porreca, M., Neri, M., Mattei, M., Funiciello, R., 2006. Fissure eruptions at Mount Vesuvius (Italy): insights on the shallow propagation of dikes at volcanoes. Geology 34 (8), 673–676. https://doi.org/10.1130/G22552.1.
Acocella, V., Neri, M., Sulpizio, R., 2009. Dike propagation within active central volcanic edifices: constraints from Somma-Vesuvius, Etna and analogue models. Bull. Volcanol. 71, 219–223. https://doi.org/10.1007/s00445-008-0258-2.
Al Shehri, A., Gudmundsson, A., 2018. Modelling of surface stresses and fracturing during dyke emplacement: application to the 2009 episode at Harrat Lunayyir, Saudi Arabia. J. Volcanol. Geoth. Res. 356, 278–303 (Half-graben).
Amadei, B., Stephansson, O., 1997. Rock Stress and its Measurement. Springer Science & Business Media.
Anderson, E.M., 1905. The dynamics of faulting. Trans. Edinb. Geol. Soc. 8 (3), 387–402.
Anderson, E.M., 1951. In: Dynamics of Faulting and Dyke Formation, second ed. Olivier and Boyd, Edinburgh.
Antoniou, V., Nomikou, P., Bardouli, P., Sorotou, P., Bonali, F., Ragia, L., Metaxas, A., 2019. The story map for Metaxa mine (Santorini, Greece): a unique site where history and volcanology meet each other. In: Proceedings of the 5th International Conference on Geographical Information Systems Theory, Applications and Management, Heraklion, Greece, 3–5 May 2019, vol. 1. SciTePress, pp. 212–219.
Apuani, T., Corazzato, C., 2009. Numerical model of the Stromboli volcano (Italy) including the effect of magma pressure in the dyke system. Rock Mech. Rock Eng. 42, 53–72.
Apuani, T., Corazzato, C., Cancelli, A., Tibaldi, A., 2005. Stability of a collapsing volcano (Stromboli, Italy): limit equilibrium analysis and numerical modelling. J. Volcanol. Geoth. Res. 144 (1–4), 191–210.
Azzaro, R., Branca, S., Gwinner, K., Coltelli, M., 2012. The volcano-tectonic map of Etna volcano, 1:100,000 scale: an integrated approach based on a morphotectonic analysis from high-resolution DEM constrained by geologic, active faulting and seismotectonic data. Italian Journal of Geosciences 131 (1), 153–170.
Barreca, G., Branca, S., Monaco, C., 2018. Three-dimensional modeling of mount Etna Volcano: volume Assessment, trend of eruption rates, and geodynamic significance. Tectonics 37 (3), 842–857.
Bazargan, M., Gudmundsson, A., 2019. Dike-induced stresses and displacements in layered volcanic zones. J. Volcanol. Geoth. Res. 384, 189–205.
Bazargan, M., Gudmundsson, A., 2020. Stresses and displacements in layered rocks induced by inclined (cone) sheets. J. Volcanol. Geoth. Res. 401, 106965.
Becerril, L., Galindo, I., Gudmundsson, A., Morales, J.M., 2013. Depth of origin of magma in eruptions. Sci. Rep. 3 (1), 1–6.
Benassi, F., Dall'Asta, E., Diotri, F., Forlani, G., Morra di Cella, U., Roncella, R., Santise, M., 2017. Testing accuracy and repeatability of UAV blocks oriented with gnss-supported aerial triangulation. Rem. Sens. 9 (2), 172.
Billi, A., Acocella, V., Funiciello, R., Giordano, G., Lanzafame, G., Neri, M., 2003. Mechanisms for ground-surface fracturing and incipient slope failure associated to the July-August 2001 eruption of Mt. Etna, Italy: analysis of ephemeral field data. J. Volcanol. Geoth. Res. 122 (3–4), 281–294.
Bistacchi, A., Tibaldi, A., Pasquarè, F.A., Rust, D., 2012. The association of cone–sheets and radial dykes: data from the Isle of Skye (UK), numerical modelling, and implications for shallow magma chambers. Earth Planet Sci. Lett. 339, 46–56.
Blaser, L., Krüger, F., Ohrnberger, M., Scherbaum, F., 2010. Scaling relations of earthquake source parameter estimates with special focus on subduction environment. Bull. Seismol. Soc. Am. 100 (6), 2914–2926.
Bonaccorso, A., Bonforte, A., Calvari, S., Del Negro, C., Di Grazia, G., Ganci, G., Neri, M., Vicari, A., Boschi, E., 2011. The initial phases of the 2008–2009 Mount Etna eruption: a multidisciplinary approach for hazard assessment. J. Geophys. Res. Solid Earth 116 (B3).
Bonafede, M., Olivieri, M., 1995. Displacement and gravity–anomaly produced by a shallow vertical dyke in a cohesionless medium. Geophys. J. Int. 123, 639–652.
Bonali, F.L., Tibaldi, A., Marchese, F., Fallati, L., Russo, E., Corselli, C., Savini, A., 2019. UAV-based surveying in volcano-tectonics: an example from the Iceland rift. J. Struct. Geol. 121, 46–64.
Bonali, F.L., Russo, E., Vitello, F., Antoniou, V., Marchese, F., Fallati, L., et al., 2021. How academics and the public experienced immersive virtual reality for geo-education. Geosciences 12 (1), 9.
Bonali, F.L., Vitello, F., Kearl, M., Tibaldi, A., Whitworth, M., Antoniou, V., et al., 2024. GeaVR: an open-source tools package for geological-structural exploration and data

collection using immersive virtual reality. Applied Computing and Geosciences 21, 100156.
Bonforte, A., Gambino, S., Neri, M., 2009. Intrusion of eccentric dikes: the case of the 2001 eruption and its role in the dynamics of Mt. Etna volcano. Special Issue: volcanoes. Tectonophysics 471, 78–86. https://doi.org/10.1016/j.tecto.2008.09.028.
Bonforte, A., Guglielmino, F., Coltelli, M., Ferretti, A., Puglisi, G., 2011. Structural assessment of Mount Etna volcano from Permanent Scatterers analysis. Geochem. Geophys. Geosyst. 12 (2).
Bonforte, A., Guglielmino, F., Puglisi, G., 2019. Large dyke intrusion and small eruption: The December 24, 2018 Mt. Etna eruption imaged by Sentinel-1 data. Terra Nova 31 (4), 405–412.
Branca, S., Coltelli, M., Groppelli, G., Lentini, F., 2011a. Geological map of Etna volcano, 1: 50,000 scale. Italian Journal of Geosciences 130 (3), 265–291. https://doi.org/10.3301/IJG.2011.15.
Branca, S., Coltelli, M., Groppelli, G., 2011b. Geological evolution of a complex basaltic stratovolcano: mount Etna, Italy. Italian Journal of Geosciences 130 (3), 306–317.
Branca, S., Musumeci, D., Ingaliso, L., 2021. The significance of the 1971 flank eruption of Etna from volcanological and historic viewpoints. Ann. Geophys. 64 (5), 543. https://doi.org/10.4401/ag-8669.
Broek, D., 1982. Elementary Engineering Fracture Mechanics. Springer Science & Business Media.
Browning, J., Gudmundsson, A., 2015. Surface displacements resulting from magma-chamber roof subsidence, with application to the 2014–2015 Bardarbunga–Holuhraun volcanotectonic episode in Iceland. J. Volcanol. Geotherm. Res. 308, 82–98.
Brunier, G., Fleury, J., Anthony, E.J., Gardel, A., Dussouillez, P., 2016. Close-range airborne Structure-from-Motion Photogrammetry for high-resolution beach morphometric surveys: examples from an embayed rotating beach. Geomorphology 261, 76–88.
Burns, J.H.R., Delparte, D., 2017. Comparison of commercial structure-from-motion photogrammetry software used for underwater three-dimensional modeling of coral reef environments. In: International Archives of the Photogrammetry, Remote Sensing and Spatial Information Sciences, vol. 42. ISPRS Archives, pp. 127–131.
Calais, E., d'Oreye, N., Albaric, J., Deschamps, A., Delvaux, D., Déverchere, J., et al., 2008. Strain accommodation by slow slip and dyking in a youthful continental rift, East Africa. Nature 456 (7223), 783–787.
Calvari, S., Tanner, L.H., Groppelli, G., Norini, G., 2004. Valle del Bove, eastern flank of Etna volcano: a comprehensive model for the opening of the depression and implications for future hazards Etna Volcano Laboratory. American Geophysical Union, 2004.
Calvari, S., Billotta, G., Bonaccorso, A., Caltabiano, T., Cappello, A., Corradino, C., Del Negro, C., Ganci, G., Neri, M., Pecora, E., Salerno, G., Spampinato, L., 2020. The VEI 2 Christmas 2018 Etna Eruption: a small but intense eruptive event or the starting phase of a larger one? Remote Sens 12, 905. https://doi.org/10.3390/rs12060905.
Cappello, A., Neri, M., Acocella, V., Gallo, G., Vicari, A., Del Negro, C., 2012. Spatial vent opening probability map of Etna volcano (Sicily, Italy). Bull. Volcanol. 74, 2083–2094.
Casu, F., Manzo, M., Lanari, R., 2006. A quantitative assessment of the SBAS algorithm performance for surface deformation retrieval from DInSAR data. Remote Sens. Environ. 102 (3–4), 195–210.
Clunes, M., Browning, J., Marquardt, C., Cortez, J., Drymoni, K., Kavanagh, J., 2023. Inclination and heterogeneity of layered geological sequences influence dike-induced ground deformation. Geology 51 (3), 278–283.
Cocina, O., Neri, G., Privitera, E., Spampinato, S., 1997. Stress tensor computations in the Mount Etna area (Southern Italy) and tectonic implications. J. Geodyn. 23 (2), 109–127.
Coltelli, M., Garduño, V.H., Neri, M., Pasquarè, G., Pompilio, M., 1994. Geology of the northern wall of the Valle del Bove, Mt Etna (Sicily). Acta Vulcanol. 5, 55–68.
Cook, K.L., 2017. An evaluation of the effectiveness of low-cost UAVs and structure from motion for geomorphic change detection. Geomorphology 278, 195–208.
Corti, N., Bonali, F.L., Russo, E., Drymoni, K., Mariotto, F.P., Gudmundsson, A., et al., 2023. Feeders vs arrested dikes: a case study from the Younger Stampar eruption in Iceland. J. Volcanol. Geoth. Res. 443, 107914.
De Beni, E., Proietti, C., Scollo, S., Cantarero, M., Mereu, L., Romeo, F., et al., 2024. A hidden eruption: the 21 may 2023 paroxysm of the Etna volcano (Italy). Rem. Sens. 16 (9), 1555.
De Novellis, V., Atzori, S., De Luca, C., Manzo, M., Valerio, E., Bonano, M., et al., 2019. DInSAR analysis and analytical modeling of Mount Etna displacements: the December 2018 volcano-tectonic crisis. Geophys. Res. Lett. 46 (11), 5817–5827.
Drymoni, K., Browning, J., Gudmundsson, A., 2020. Dyke-arrest scenarios in extensional regimes: insights from field observations and numerical models, Santorini, Greece. J. Volcanol. Geoth. Res. 396, 106854.
Drymoni, K., Browning, J., Gudmundsson, A., 2021. Volcanotectonic interactions between inclined sheets, dykes, and faults at the Santorini Volcano, Greece. J. Volcanol. Geoth. Res. 107294.
Drymoni, K., Browning, J., Gudmundsson, A., 2022. Spatial and temporal volcanotectonic evolution of Santorini volcano, Greece. Bull. Volcanol. 84 (6), 60.
Drymoni, K., Russo, E., Tibaldi, A., Corti, N., Bonali, F.L., Mariotto, F.P., 2023. Dyke-induced graben formation in a heterogeneous succession on Mt. Etna: insights from field observations and FEM numerical models. J. Volcanol. Geoth. Res. 433, 107712.
Dundurs, J., 1969. Edge-bonded dissimilar orthogonal wedges. J. Appl. Mech. 36, 650–652.
Ebinger, C., Ayele, A., Keir, D., Rowland, J., Yirgu, G., Wright, T., Belachew, M., Hamling, I., 2010. Length and timescales of rift faulting and magma intrusion: the Afar rifting cycle from 2005 to present. Annu. Rev. Earth Planet Sci. 38, 439–466.
Esposito, G., Mastrorocco, G., Salvini, R., Oliveti, M., Starita, P., 2017. Application of UAV photogrammetry for the multi-temporal estimation of surface extent and volumetric excavation in the Sa Pigada Bianca open-pit mine, Sardinia, Italy. Environ. Earth Sci. 76, 103. https://doi.org/10.1007/s12665-017-6409-z.
Fallati, L., Saponari, L., Savini, A., Marchese, F., Corselli, C., Galli, P., 2020. Multi-Temporal UAV data and object-based image analysis (OBIA) for estimation of substrate changes in a post-bleaching scenario on a Maldivian reef. Rem. Sens. 12, 2093.
Falsaperla, S., Neri, M., 2015. Seismic footprints of shallow dyke propagation at Etna, Italy. Sci. Rep. 5 (1), 1–9.
Ferrari, L., Garduño, V.H., Neri, M., 1991. I dicchi della Valle del Bove, Etna: un metodo per stimare le dilatazioni di un apparato vulcanico. Memor. Soc. Geol. Ital. 47, 495–508.
Fischer, T., Hrubcová, P., Salama, A., Doubravová, J., Ágústsdóttir, T., Gudnason, E.Á., et al., 2022. Swarm seismicity illuminates stress transfer prior to the 2021 Fagradalsfjall eruption in Iceland. Earth Planet Sci. Lett. 594, 117685.
Folch, A., Martı, J., 2004. Geometrical and mechanical constraints on the formation of ring-fault calderas. Earth Planet Sci. Lett. 221 (1–4), 215–225.
Forslund, T., Gudmundsson, A., 1992. Structure of tertiary and pleistocene normal faults in Iceland. Tectonics 11 (1), 57–68.
Fossen, H., 2016. Structural Geology. Cambridge university press.
Galindo, I., Gudmundsson, A., 2012. Basaltic feeder dykes in rift zones: geometry, emplacement, and effusion rates. Nat. Hazards Earth Syst. Sci. 12 (12), 3683–3700.
Galland, O., Holohan, E., de Vries, B.V.W., Burchardt, S., 2015. Laboratory modelling of volcano plumbing systems: a review. Physical Geology of Shallow Magmatic Systems 147–214.
Gambino, S., Barreca, G., Bruno, V., De Guidi, G., Ferlito, C., Gross, F., et al., 2022. Transtension at the northern termination of the alfeo-etna fault system (western ionian sea, Italy): seismotectonic implications and relation with Mt. Etna volcanism. Geosciences 12 (3), 128.
Garagash, D., Detournay, E., 2000. The tip region of a fluid-driven fracture in an elastic medium. ASME Journal of Applied Mechanics 67, 183–192.
Garduño, V.H., Neri, M., Pasquarè, G., Borgia, A., Tibaldi, A., 1997. Geology of NE-rift of mount Etna, sicily (Italy). Acta Vulcanol. 9 (1/2), 91–100.
Gerloni, I.G., Carchiolo, V., Vitello, F.R., Sciacca, E., Becciani, U., Costa, A., Riggi, S., Bonali, F.L., Russo, E., Fallati, L., Marchese, F., Tibaldi, A., 2018. Immersive virtual reality for Earth Sciences. In: Proceedings of the 2018 Federated Conference on Computer Science and Information Systems (FedCSIS). IEEE, Poznan, Poland, pp. 527–534, 9–12 September 2018.
Geshi, N., Neri, M., 2014. Dynamic feeder dyke systems in basaltic volcanoes: the exceptional example of the 1809 Etna eruption (Italy). Frontiers in Earth Scices 2, 13. https://doi.org/10.3389/feart.2014.00013.
Gomez, C., Hayakawa, Y., Obanawa, H., 2015. A study of Japanese landscapes using structure from motion derived DSMs and DEMs based on historical aerial photographs: new opportunities for vegetation monitoring and diachronic geomorphology. Geomorphology 242, 11–20.
Grandin, R., Socquet, A., Binet, R., Klinger, Y., Jacques, E., De Chabalier, J.B., King, G.C.P., Lasserre, C., Tait, S., Tapponnier, P., Delorme, A., Pinzuti, P., 2009. September 2005 Manda Hararo-Dabbahu rifting event, Afar (Ethiopia): constraints provided by geodetic data. J. Geophys. Res. Solid Earth 114 (B8).
Grandin, R., Socquet, A., Jacques, E., Mazzoni, N., De Chabalier, J.B., King, G.C.P., 2010. Sequence of rifting in Afar, Manda-Hararo rift, Ethiopia, 2005–2009: time-space evolution and interactions between dikes from interferometric synthetic aperture radar and static stress change modeling. J. Geophys. Res. Solid Earth 115 (B10).
Grant, J.V., Kattenhorn, S.A., 2004. Evolution of vertical faults at an extensional plate boundary, southwest Iceland. J. Struct. Geol. 26 (3), 537–557.
Graue, B., Siegesmund, S., Middendorf, B., 2011. Quality assessment of replacement stones for the Cologne Cathedral: mineralogical and petrophysical requirements. Environ. Earth Sci. 63, 1799–1822.
Griffith, A.A., 1924. In: Proceedings of the First International Congress on Applied Mechanics. delft. J. Waltman Jr, Delft, pp. 55–63.
Grosfils, E.B., 2007. Magma reservoir failure on the terrestrial planets: assessing the importance of gravitational loading in simple elastic models. J. Volcanol. Geoth. Res. 166 (2), 47–75.
Gudmundsson, A., 1986. Formation of crystal magma chambers in Iceland. Geology 14 (2), 164–166.
Gudmundsson, A., 1998. Formation and development of normal-fault calderas and the initiation of large explosive eruptions. Bull. Volcanol. 60, 160–170.
Gudmundsson, A., 2003. Surface stresses associated with arrested dykes in rift zones. Bull. Volcanol. 65, 606–619.
Gudmundsson, A., 2011a. Rock Fractures in Geological Processes. Cambridge University Press.
Gudmundsson, A., 2011b. Deflection of dykes into sills at discontinuities and magma-chamber formation. Tectonophysics 500 (1–4), 50–64.
Gudmundsson, A., 2020. Volcanotectonics: Understanding the Structure, Deformation and Dynamics of Volcanoes. Cambridge University Press.
Gudmundsson, A., Bäckström, K., 1991. Structure and development of the Sveinagja graben, Northeast Iceland. Tectonophysics 200 (1–3), 111–125.
Gudmundsson, A., De Guidi, G., Scudero, S., 2013. Length–displacement scaling and fault growth. Tectonophysics 608, 1298–1309.
Guldstrand, F., Burchardt, S., Hallot, E., Galland, O., 2017. Dynamics of surface deformation induced by dikes and cone sheets in a cohesive Coulomb brittle crust. J. Geophys. Res. Solid Earth 122 (10), 8511–8524.
Hafner, W., 1951. Stress distributions and faulting. Geol. Soc. Am. Bull. 62 (4), 373–398.

Haimson, B.C., Rummel, F., 1982. Hydrofracturing stress measurements in the Iceland research drilling project drill hole at Reydarfjordur, Iceland. J. Geophys. Res. Solid Earth 87 (B8), 6631–6649.
Heap, M.J., Villeneuve, M., Albino, F., Farquharson, J.I., Brothelande, E., Amelung, F., et al., 2020. Towards more realistic values of elastic moduli for volcano modelling. J. Volcanol. Geoth. Res. 390, 106684.
Hjartardóttir, Á.R., Einarsson, P., Gudmundsson, M.T., Högnadóttir, T., 2016. Fracture movements and graben subsidence during the 2014 Bárðarbunga dike intrusion in Iceland. J. Volcanol. Geoth. Res. 310, 242–252.
Hoek, E., Diederichs, M.S., 2006. Empirical estimation of rock mass modulus. International journal of rock mechanics and mining sciences 43 (2), 203–215.
James, M.R., Robson, S., 2012. Straightforward reconstruction of 3D surfaces and topography with a camera: accuracy and geoscience application. J. Geophys. Res. Solid Earth 117, F03017. https://doi.org/10.1029/2011JF002289.
James, M.R., Robson, S., d'Oleire-Oltmanns, S., Niethammer, U., 2017. Optimising UAV topographic surveys processed with structure-from-motion: ground control quality, quantity and bundle adjustment. Geomorphology 280, 51–66.
Kavanagh, J.L., Menand, T., Sparks, R.S.J., 2006. An experimental investigation of sill formation and propagation in layered elastic media. Earth Planet Sci. Lett. 245 (3–4), 799–813.
Kieffer, G., 1975. Sur l'existence d'une rift zone à l'Etna. CR Acad Sci Paris 280 (D), 263–266.
Kieffer, G., 1985. Evolution structurale et dynamique d'un grand volcan polygenique: Stades d'edification et activite actuelle de l'Etna (Sicile). Univ. Clermont Fd, Thesis.
Le Guern, F., 1972. Etudes dynamique sur la phase gazeuse eruptive, Thèse de 3ème cycle, R 4383, C.E.N. Saclay, Gif sur Yvette.
Lo Giudice, E., Patanè, G., Rasà, R., Romano, R., 1982. The structural framework of Mount Etna. Memor. Soc. Geol. Ital. 23, 125–158.
Magee, C., Jackson, C.A.L., 2021. Can we relate the surface expression of dike-induced normal faults to subsurface dike geometry? Geology 49 (4), 366–371.
Marinos, V.I.I.I., Marinos, P., Hoek, E., 2005. The geological strength index: applications and limitations. Bull. Eng. Geol. Environ. 64, 55–65.
Mastin, L.G., Pollard, D.D., 1988. Surface deformation and shallow dike intrusion processes at Inyo Craters, Long Valley, California. J. Geophys. Res. 13221–13235.
McGuire, W.J., Pullen, A.D., 1989. Location and orientation of eruptive fissures and feeder dykes at Mount Etna; influence of gravitational and regional tectonic stress regimes. J. Volcanol. Geoth. Res. 38 (3–4), 325–344.
Monaco, C., De Guidi, G., Ferlito, C., 2010. The morphotectonic map of Mt. Etna. Italian Journal of Geosciences 129 (3), 408–428.
Murray, J.B., Pullen, A.D., 1984. Three-dimensional model of the feeder conduit of the 1983 eruption of Mt. Etna volcano, from ground deformation measurements. Bull. Volcanol. 47, 1145–1163.
Neri, M., Acocella, V., 2006. The 2004–2005 Etna eruption: implications for flank deformation and structural behaviour of the volcano. J. Volcanol. Geoth. Res. 158, 195–206. https://doi.org/10.1016/j.jvolgeores.2006.04.022.
Neri, M., Lanzafame, G., 2009. Structural features of the 2007 Stromboli eruption. J. Volcanol. Geoth. Res. 182, 137–144. https://doi.org/10.1016/j.jvolgeores.2008.07.021.
Neri, M., Garduño, V.H., Pasquarè, G., Rasà, R., 1991. Studio strutturale e modello cinematico della Valle del Bove. Acta Vulcanol. 1, 17–24.
Neri, M., Acocella, V., Behncke, B., 2004. The role of the Pernicana fault system in the spreading of mount Etna (Italy) during the 2002-2003 eruption. Bull. Volcanol. 66, 417–430. https://doi.org/10.1007/s00445-003-0322-x.
Neri, M., Guglielmino, F., Rust, D., 2007. Flank instability on Mount Etna: Radon, radar interferometry, and geodetic data from the southwestern boundary of the unstable sector. J. Geophys. Res. Solid Earth 112 (B4).
Neri, M., Lanzafame, G., Acocella, V., 2008. Dike emplacement and related hazard in volcanoes with sector collapse: the 2007 Stromboli eruption. Journal of Geological Society of London 165, 883–886. https://doi.org/10.1144/0016-76492008-002.
Neri, M., Casu, F., Acocella, V., Solaro, G., Pepe, S., Berardino, P., Sansosti, E., Caltabiano, T., Lundgren, P., Lanari, R., 2009. Deformation and eruptions at Mt. Etna (Italy): a lesson from 15 years of observations. Geophys. Res. Lett. 36, L02309 https://doi.org/10.1029/2008GL036151.
Neri, M., Acocella, V., Behncke, B., Giammanco, S., Mazzarini, F., Rust, D., 2011. Structural analysis of the eruptive fissures at Mount Etna (Italy). Ann. Geophys.
Nobile, A., Pagli, C., Keir, D., Wright, T.J., Ayele, A., Ruch, J., Acocella, V., 2012. Dike-fault interaction during the 2004 Dallol intrusion at the northern edge of the Erta Ale Ridge (Afar, Ethiopia). Geophys. Res. Lett. 39 (19).
Pallister, J.S., McCausland, W.A., Jónsson, S., Lu, Z., Zahran, H.M., Hadidy, S.E., Aburukbah, A., Stewart, I.C.F., Lundgren, P.R., White, R.A., Moufti, M.R., 2010. Broad accommodation of rift-related extension recorded by dyke intrusion in Saudi Arabia. Nat. Geosci. 3 (10), 705–712 (Half-graben).
Patanè, D., Aliotta, M., Cannata, A., Cassisi, C., Coltelli, M., Di Grazia, G., et al., 2011. Interplay between Tectonics and Mount Etna's volcanism: insights into the geometry of the plumbing system. In: New Frontiers in Tectonic Research-At the Midst of Plate Convergence. InTech.
Perras, M.A., Diederichs, M.S., 2014. A review of the tensile strength of rock: concepts and testing. Geotech. Geol. Eng. 32, 525–546.
Philipp, S.L., Afşar, F., Gudmundsson, A., 2013. Effects of mechanical layering on hydrofracture emplacement and fluid transport in reservoirs. Front. Earth Sci. 1, 4.
Pollard, D.D., Delaney, P.T., Duffield, W.A., Endo, E.T., Okamura, A.T., 1983. Surface deformation in volcanic rift zones. In: Developments in Geotectonics, vol. 19. Elsevier, pp. 541–584.
Ramsay, J.G., Lisle, R.J., 2000. Applications of Continuum Mechanics in Structural Geology (Techniques of Modern Structural Geology, vol. 3. Academic Press vol. 3.
Rivas-Dorado, S., Ruíz, J., Romeo, I., 2023. Modeling of dike-induced graben nucleation in the Elysium region, Mars: the role of planetary gravity. J. Struct. Geol. 167, 104778.
Rowland, J.V., Baker, E., Ebinger, C.J., Keir, D., Kidane, T., Biggs, J., Hayward, N., Wright, T.J., 2007. Fault growth at a nascent slow-spreading ridge: 2005 Dabbahu rifting episode. Afar. Geophysical Journal International 171 (3), 1226–1246.
Rubin, A.M., 1992. Dike-induced faulting and graben subsidence in volcanic rift zones. J. Geophys. Res. Solid Earth 97 (B2), 1839–1858.
Rubin, A.M., 1995. Propagation of magma-filled crack. Annu. Rev. Earth Planet Sci. 23, 287–336.
Rubin, A.M., Pollard, D.D., 1987. Origins of blade-like dikes in volcanic rift zones. In: Decker, R.W., Wight, T.L., Stuffer, P.H. (Eds.), Volcanism in Hawaii, vol. 1350. US Geological Survey Professional Papers, pp. 1449–1470.
Rubin, A.M., Pollard, D.D., 1988. Dike-induced faulting in rift zones of Iceland and Afar. Geology 16 (5), 413–417.
Ruch, J., Pepe, S., Casu, F., Acocella, V., Neri, M., Solaro, G., Sansosti, E., 2012. How do rift zones relate to volcano flank instability? Evidence from collapsing rifts at Etna. Geophys. Res. Lett. 39, L20311 https://doi.org/10.1029/2012GL053683.
Ruch, J., Pepe, S., Casu, F., Solaro, G., Pepe, A., Acocella, V., Neri, M., Sansosti, E., 2013. Seismo-tectonic behavior of the Pernicana Fault System (Mt Etna): a gauge for volcano flank instability? J. Geophys. Res. Solid Earth 118, 4398–4409. https://doi.org/10.1002/jgrb.50281.
Ruch, J., Wang, T., Xu, W., Hensch, M., Jónsson, S., 2016. Oblique rift opening revealed by reoccurring magma injection in central Iceland. Nat. Commun. 7 (1), 12352.
Schiefer, E., Gilbert, R., 2007. Reconstructing morphometric change in a proglacial landscape using historical aerial photography and automated DEM generation. Geomorphology 88 (1–2), 167–178.
Schultz, R., 1995. Limits on strength and deformation properties of jointed basaltic rock masses. Rock Mech. Rock Eng. 28 (1), 1–15.
Scudero, S., De Guidi, G., Gudmundsson, A., 2019. Size distributions of fractures, dykes, and eruptions on Etna, Italy: implications for magma-chamber volume and eruption potential. Sci. Rep. 9 (1), 4139.
Sigmundsson, F., Hooper, A., Hreinsdóttir, S., Vogfjörd, K.S., Ófeigsson, B.G., Heimisson, E.R., et al., 2015. Segmented lateral dyke growth in a rifting event at Bárðarbunga volcanic system, Iceland. Nature 517 (7533), 191–195.
Sigurdsson, O., 1980. Surface deformation of the Krafla fissure swarm in two rifting events. J. Geophys. 47 (1), 154–159.
Siniscalchi, A., Tripaldi, S., Neri, M., Balasco, M., Romano, G., Ruch, J., Schiavone, D., 2012. Flank instability structure of Mt Etna inferred by a magnetotelluric survey. J. Geophys. Res. 117, B03216 https://doi.org/10.1029/2011JB008657, 2012.
Smith, M.W., Carrivick, J.L., Quincey, D.J., 2016. Structure from motion photogrammetry in physical geography. Prog. Phys. Geogr. 40, 247–275.
Solaro, G., Acocella, V., Pepe, S., Ruch, J., Neri, M., Sansosti, E., 2010. Anatomy of an unstable volcano through InSAR data: multiple processes affecting flank instability at Mt. Etna in 1994-2008. J. Geophys. Res. 115, B10405 https://doi.org/10.1029/2009JB000820.
Tentler, T., 2005. Propagation of brittle failure triggered by magma in Iceland. Tectonophysics 406 (1–2), 17–38.
Thatcher, W., Hill, D.P., 1995. A simple model for fault generated morphology of slow-spreading mid-ocean ridges. J. Geophys. Res. 100, 561–570.
Tibaldi, A., 1996. Mutual influence of dyking and collapses at Stromboli volcano, Italy. Geological Society, London, Special Publications 110 (1), 55–63.
Tibaldi, A., 2001. Multiple sector collapses at Stromboli volcano, Italy: how they work. Bull. Volcanol. 63, 112–125.
Tibaldi, A., 2003. Influence of cone morphology on dykes, Stromboli, Italy. J. Volcanol. Geoth. Res. 126 (1–2), 79–95.
Tibaldi, A., 2004. Major changes in volcano behaviour after a sector collapse: insights from Stromboli, Italy. Terra. Nova 16 (1), 2–8.
Tibaldi, A., 2015. Structure of volcano plumbing systems: a review of multi-parametric effects. J. Volcanol. Geoth. Res. 298, 85–135.
Tibaldi, A., Groppelli, G., 2002. Volcano-tectonic activity along structures of the unstable NE flank of Mt. Etna (Italy) and their possible origin. J. Volcanol. Geoth. Res. 115 (3–4), 277–302.
Tibaldi, A., Bonali, F.L., Russo, E., Fallati, L., 2020a. Surface deformation and strike-slip faulting controlled by dyking and host rock lithology: a compendium from the Krafla Rift, Iceland. J. Volcanol. Geoth. Res. 395, 106835.
Tibaldi, A., Bonali, F.L., Vitello, F., Delage, E., Nomikou, P., Antoniou, V., Becciani, U., Van Wyk de Vries, B., Krokos, M., Whitworth, M., 2020b. Real world-based immersive Virtual Reality for research, teaching and communication in volcanology. Bull. Volcanol. 82, 38.
Tibaldi, A., Bonali, F.L., Corti, N., Russo, E., Drymoni, K., De Beni, E., Branca, S., Neri, M., Cantarero, M., Pasquaré Mariotto, F., 2022. Surface deformation during the 1928 fissure eruption of Mt. Etna (Italy): insights from field data and FEM numerical modelling. Tectonophysics 837, 229468.
Trippanera, D., Acocella, V., Ruch, J., 2014. Dike-induced contraction along oceanic and continental divergent plate boundaries. Geophys. Res. Lett. 41 (20), 7098–7104.
Trippanera, D., Ruch, J., Acocella, V., Rivalta, E., 2015a. Experiments of dike-induced deformation: insights on the long-term evolution of divergent plate boundaries. J. Geophys. Res. Solid Earth 120 (10), 6913–6942.
Trippanera, D., Acocella, V., Ruch, J., Abebe, B., 2015b. Fault and graben growth along active magmatic divergent plate boundaries in Iceland and Ethiopia. Tectonics 34 (11), 2318–2348.
Trippanera, D., Ruch, J., Passone, L., Jónsson, S., 2019. Structural mapping of dike-induced faulting in Harrat Lunayyir (Saudi Arabia) by using high resolution drone imagery. Front. Earth Sci. 7, 168 (Half-graben).

Turner, D., Lucieer, A., Watson, C., 2012. An automated technique for generating georectified mosaics from ultra-high resolution unmanned aerial vehicle (UAV) imagery, based on structure from motion (SfM) point clouds. Rem. Sens. 4 (5), 1392–1410.
Verhoeven, G., 2011. Taking computer vision aloft–archaeological three-dimensional reconstructions from aerial photographs with photoscan. Archaeol. Prospect. 18, 67–73.
Vezzoli, L., Tibaldi, A., Renzulli, A., Menna, M., Flude, S., 2008. Faulting-assisted lateral collapses and influence on shallow magma feeding system at Ollagüe volcano (Central Volcanic Zone, Chile-Bolivia Andes). J. Volcanol. Geoth. Res. 171 (1–2), 137–159.
Vollgger, S.A., Cruden, A.R., 2016. Mapping folds and fractures in basement and cover rocks using UAV photogrammetry, Cape Liptrap and Cape Paterson, Victoria, Australia. J. Struct. Geol. 85, 168–187.
Warpinski, H.R., 1985. Measurement of width and pressure in a propagating hydraulic fracture. J. Soc. Petrol. Eng 46–54.
Wells, D.L., Coppersmith, K.J., 1994. New empirical relationships among magnitude, rupture length, rupture width, rupture area, and surface displacement. Bull. Seismol. Soc. Am. 84 (4), 974–1002.
Westoby, M.J., Brasington, J., Glasser, N.F., Hambrey, M.J., Reynolds, J.M., 2012. "Structure-from-Motion" photogrammetry: a low-cost, effective tool for geoscience applications. Geomorphology 179, 300–314.
Wright, T.J., Ebinger, C., Biggs, J., Ayele, A., Yirgu, G., Keir, D., Stork, A., 2006. Magma-maintained rift segmentation at continental rupture in the 2005 Afar dyking episode. Nature 442 (7100), 291–294.
Xu, W., Jónsson, S., Corbi, F., Rivalta, E., 2016. Graben formation and dike arrest during the 2009 Harrat Lunayyir dike intrusion in Saudi Arabia: insights from InSAR, stress calculations and analog experiments. J. Geophys. Res. Solid Earth 121 (4), 2837–2851.